



Bernardo Garcia Caetano

Bachelor of Science in Micro and Nanotechnologies Engineering

Study of P(VDF-TrFE) for Structures via 3D Printing

Dissertation submitted in partial fulfilment of the requirements for the degree of
Master of Science in Micro and Nanotechnologies Engineering

Adviser: Professor Doutor Rui Alberto Garção Barreira do Nascimento
Igreja, Assistant Professor, FCT-UNL

Co-adviser: Professor Doutor Pedro Miguel Cândido Barquinha,
Associate Professor, FCT-UNL

Chair Prof. Dr Rodrigo Martins

Rapporteurs Prof. Dr Maria do Carmo Lança

Member Prof. Dr Rui Igreja

December, 2019

Study of P(VDF-TrFE) for Structures via 3D Printing

Copyright ©Bernardo Garcia Caetano, Faculdade de Ciências e Tecnologia, Universidade Nova de Lisboa.

A Faculdade de Ciências e Tecnologia e a Universidade Nova de Lisboa têm o direito, perpétuo e sem limites geográficos, de arquivar e publicar esta dissertação através de exemplares impressos reproduzidos em papel ou de forma digital, ou por qualquer outro meio conhecido ou que venha a ser inventado, e de a divulgar através de repositórios científicos e de admitir a sua cópia e distribuição com objetivos educacionais ou de investigação, não comerciais, desde que seja dado crédito ao autor e editor.

“The only true wisdom is in knowing you know nothing.”

Socrates

Acknowledgements

Com o fim de mais uma etapa educativa e pessoal, utilizo esta página da minha dissertação para agradecer a quem contribuiu para que o meu percurso académico corresse da melhor forma.

Começo por agradecer à Faculdade de Ciências e Tecnologias da Universidade Nova de Lisboa, a grande instituição da qual tenho orgulho em dizer que fiz parte e a qual contribui para a pessoa que sou hoje com as suas condições, docentes e os demais.

De seguida, um agradecimento ao professor Rodrigo Martins e à professora Elvira Fortunato pela criação e investimento no curso de Engenharia de Micro e Nanotecnologias e nos seus alunos, mostrando total confiança nestes e no seu trabalho. Ainda sem esquecer, um agradecimento ao Departamento de Ciências dos Materiais, CENIMAT e CEMOP e às pessoas que nele trabalham e que me ajudaram não só durante o curso, mas também nesta fase importante da dissertação, com a ajuda na ambientação aos laboratórios e com o bom ambiente nos laboratórios. Um agradecimento ao projeto 1D-Neon pelos materiais e equipamentos financiados no âmbito desta dissertação, sem os quais não seria possível.

Aos professores Rui Igreja e Pedro Barquinha, meu orientador e co-orientador, pelo conhecimento transmitido, apoio e ajuda durante toda esta etapa. Ainda um agradecimento ao professor Carlos Dias pelo seu conhecimento e disponibilidade para me ajudar numa parte tão importante desta dissertação.

Antes de mais, quero agradecer em especial aos meus pais por me terem dado a oportunidade estudar a este nível com o apoio logístico, financeiro e pessoal que me deram e que me permitiu chegar onde estou. Ao meu irmão um grande obrigado pela picardia saudável que me fez concluir esta etapa com sucesso.

Quero aproveitar para agradecer a todos os amigos que fiz ao longo do curso e dos quais me vou sempre recordar, deixando algum destaque para a grupeta da festança que inclui o Matinhos Matex, a Pina, o Johny, o Toninho, a Carol, o Frederico, o Mc Big Head, o Dj Rebordation, o Sabinex, o Ricardo dos gafanhotos, o Rolo, o PRIMO Diogo, o não padrinho Nuno, o Neto, o Opinião, a Açoreana, a Mariana, o Ferreira, o Castelo, o Luís, o Renato e outros tantos que quando havia festa lá estavam eles. Ainda agradecer ao Carlos Dias e à Glória pelos mais variados momentos marcantes e divertidos ao longo do curso e ainda ao Chico Matos por ter sido um bom senhorio nas minhas estadias.

Um ainda especial obrigado a 3 pessoas que me marcaram bastante nesta passagem por este curso que são a Marta, o Ramos e o Recife. Foram uma madrinha, padrinho e padrinho adotado cinco estrelas e como muitos não se podem gabar, sempre preocupados, interessados e disponíveis.

Deixo para o fim a Inês, a pessoa que mais aturou o meu mau humor nos meus dias maus e stressantes nos quais tinha sempre as palavras certas para me animar, bem como me aturou nos meus dias bons em que partilhava da minha felicidade quando as coisas corriam bem, quer fosse no âmbito da faculdade ou no âmbito mais pessoal. Agradeço-te pela paciência que tiveste comigo e pelo apoio que foste! Obrigado!

Abstract

This work is focussed on using additive manufacturing (AM) to produce electroactive structures using fused deposition modelling (FDM) and P(VDF-TrFE) as a ferroelectric polymer which will confer electroactive properties to printed structures. The FDM, commonly called 3D printing, was chosen due to its emergence in the industry segment with low-cost production and the capability of projecting prototypes without shape limitations, converting a digital design in a physical object. Beyond these features, the possibility of using functional materials and their properties in the production of sensors and actuators was one of the main reasons for the increased interest in this technology.

The boundaries of 3D printing process were explored during the production in order to obtain a uniform and homogenous thin film. It was used a P(VDF-TrFE) filament that was previously extruded to make possible the use of additive manufacturing process. Subsequently, a commercial conductive PLA filament was used to produce electrodes for the electrical characterization of the electroactive films.

P(VDF-TrFE) films with 65 μm and aluminium electrodes yielded the best results with a pyroelectric coefficient of $3 \mu\text{C m}^{-2} \text{K}^{-1}$. The aforementioned sample was used to produce a fully 3D printable pyroelectric sensor. This sensor was made of P(VDF-TrFE), commercial conductive PLA and conventional PLA. The P(VDF-TrFE) provides electroactive properties, conductive PLA enables the creation of conductive tracks and the conventional PLA gave structural basis to the device.

Keywords: Additive manufacturing, 3D printing, P(VDF-TrFE), electroactive materials.

Resumo

Este trabalho foca-se no uso da fabricação aditiva para a produção de estruturas eletroativas usando a modelagem de deposição fundida (MDF) e o P(VDF-TrFE) como polímero ferroelétrico que confere as propriedades eletroativas às estruturas impressas. A MDF, normalmente chamado de impressão 3D, foi escolhida devido ao seu impacto na indústria com os baixos custos de produção e a capacidade de projetar protótipos sem limitações na forma, convertendo um desenho digital numa peça física. Para além destas características, uma das principais razões para o crescente interesse nesta tecnologia foi a possibilidade de usar materiais funcionais que permitem a incorporação de sensores e atuadores.

De forma a obter um filme fino, uniforme e homogéneo foram testados os limites da impressora 3D durante a produção, usando um filamento de P(VDF-TrFE) previamente extrudido de forma a possibilitar o uso de um processo de fabricação aditiva. Posteriormente, foi usado um filamento comercial de PLA condutor para produzir elétrodos necessários para a caracterização elétrica dos filmes de material eletroativo e conexões elétricas dos dispositivos.

Os dispositivos com elétrodos de alumínio foram os que mostraram melhores resultados apresentando um coeficiente piroelétrico de $3 \mu\text{C m}^{-2} \text{K}^{-1}$ para amostras com $65 \mu\text{m}$ de espessura. Com os resultados obtidos, esta configuração foi usada para produzir uma estrutura totalmente impressa que incorpora um sensor piroelétrico. Este sensor é composto por P(VDF-TrFE), PLA condutor comercial e PLA convencional. Neste dispositivo, o P(VDF-TrFE) confere as propriedades eletroativas, o PLA condutor permite a criação de pistas condutoras e PLA convencional dá estrutura ao dispositivo.

Palavras-chave: Fabricação aditiva, impressão 3D, P(VDF-TrFE), materiais eletroativos.

Abbreviations

3D	Three dimensional
3DP	Three dimensional printing
ABS	Acrylonitrile butadiene styrene
AM	Additive Manufacturing
AOA	One layer film with ironing between two evaporated electrodes of aluminium
a.u.	Arbitrary unit
BS	Bottom Surface
BTO	Barium titanate
COC	One layer film with ironing between two conductive PLA electrodes printed separately
CPLA	Conductive PLA
DSC	Differential Scanning Calorimetry
EAP	Electroactive polymers
EDS	Energy Dispersive Spectroscopy
EEAP	Electronic electroactive polymers
EPAM	Electric polling assisted additive manufacturing
FDM	Fused Deposition Modelling
FFF	Fused Filament Fabrication
FOM	Figure of Merit
FTIR	Fourier-Transform Infrared Spectroscopy
GPIB	General Purpose Interface Bus
HT	Hotplate at 155 °C
IEAP	Ionic electroactive polymers
MFI	Melt Flow Index
OLF	One layer film
OLFI	One layer printed film with ironing
PC	Computer
PCOC	One layer film with ironing with a printed electrode of conductive PLA and an conductive PLA electrode printed separately
PLA	Poly lactide
PVDF	Polyvinylidene fluoride
P(VDF-TrFE)	Poly(vinylidene fluoride-trifluoroethylene)
RT	Room temperature
TG⁺TG⁻	<i>Trans-gauche-trans-gauche</i> phase
TLPF	Two layers pressed film
TS	Top Surface
TTT	<i>All-trans</i> phase
TTTG⁺TTTG⁻	<i>All-trans-gauche-all-trans-gauche</i> phase
XRD	X-Ray Diffraction

Symbols

Δt	Period of time
ΔT	Variation of temperature
ϵ_0	Vacuum permittivity ($8.854 \times 10^{-12} \text{ F m}^{-1}$)
ϵ_r	Relative permittivity
ρ	Resistivity
A	Area
D	Strain constant
d_{33}	Induced strain in direction 3 per unit electric field applied in direction 3
E_c	Coercive field
F_v	Figure of merit for a sensor with a voltage read-out circuit
i_p	Pyroelectric current
k_{33}	Electromechanical coupling factor
L	Length
p_i	Pyroelectric coefficient
P_r	Remanent polarisation
Q	Pyroelectric charge
R	Resistance
R_{sh}	Sheet resistance
T	Thickness
T_c	Curie temperature
$\text{tg } \delta$	Loss tangent
V_{out}	Output voltage
W	Width

Table of contents

<i>Abstract</i>	ix
<i>Resumo</i>	xi
<i>Abbreviations</i>	xiii
<i>Symbols</i>	xv
<i>List of Figures</i>	xix
<i>List of Tables</i>	xxi
Motivation and objectives.....	1
Chapter I.Introduction.....	3
1. Fused deposition modelling.....	3
1.1. Working principle of FDM	3
1.2. FDM vs Traditional manufacturing techniques	3
2. Extrusion fundamentals	4
3. Functional materials	5
3.1. Electroactive polymers	5
3.2. Ferroelectric, pyroelectric and piezoelectric materials	6
3.3. Ferroelectric polymers	6
4. Fused deposition modelling of ferroelectric polymers	7
Chapter II.Materials and Methods.....	9
1. Materials	9
1.1. P(VDF-TrFE).....	9
1.2. Conductive PLA Proto-Pasta.....	9
2. Sample production.....	9
2.1. Fibre extrusion and filament production	9
2.2. 3D Printing of P(VDF-TrFE) film	10
2.3. 3D Printing of conductive PLA Proto-Pasta samples to study sheet resistance	10
2.4. 3D Printing of conductive PLA Proto-Pasta electrodes	10
2.5. Evaporation of aluminium electrodes in P(VDF-TrFE) film.....	11
3. Sample characterization	11
3.1. Structural, chemical and morphological characterization	11
4. Electrical characterization.....	11
4.1. Polarisation	11
4.2. Measurement of pyroelectric properties	12
4.3. Measurement of capacitance	13
5. Device production and experiments	13
Chapter III.Results and Discussion.....	15
1. Conductive PLA characterization	15

1.1. Study of sheet resistance	15
1.2. Characterization of 3D printed electrodes	17
2. P(VDF-TrFE) characterization	18
2.1. Morphological characterizations of films	18
2.2. DSC characterization of pellet, fibre, two layers pressed film and one layer film with ironing.....	20
2.3. FTIR characterization of pellet, fibre, two layers pressed film and one layer film with ironing.....	21
2.4. XRD characterization of pellet, fibre, two layers pressed film and one layer film with ironing.....	22
2.5. Summary of two layers pressed film and one layer film with ironing characterization ..	23
3. Sample Characterization	23
3.1. Capacitance measurements.....	23
3.2. Polarisation experiments	24
3.3. Pyroelectric coefficient and Figure of Merit	27
4. Pyroelectric device experiments.....	29
Chapter IV.Conclusion	31
References.....	33
Appendices	39
A. PVDF and P(VDF-TrFE) molecular structures	39
B. Additional information about used materials	40
C. Parameters of 3D printing.....	41
D. Rectifying circuit used in polarisation setup	42
E. Measurement circuit used during the polarisation	43
F. Polarisation process	44
G. Measurement of pyroelectric response	45
H. Measurement of capacitance	46
I. 3D model device	47
J. Experimental setup.....	48
K. Morphological analysis of sheet resistance samples	49

List of Figures

Figure 1. Schematic diagram of the FDM process based on [4].	3
Figure 2. Ferroelectric a) phase transition of ferroelectric to paraelectric b) polarization hysteresis from [30].	6
Figure 3. Used setup in samples polarisation.	12
Figure 4. Used setup in measurements of pyroelectric properties of samples.	12
Figure 5. Study of sheet resistance with the increasing of the number of layers and comparison between the room temperature dry process of silver conductive ink electrodes with dry of 3 min in hotplate at 155 °C.	15
Figure 6. Morphological images of the top and bottom surfaces of used sheet resistance samples, with a different number of layers and different dry processes.	16
Figure 7. Morphological characterization of the 3D printed electrode.	17
Figure 8. SEM-EDS of 3D printed electrodes of a) top surface, and b) bottom surface.	18
Figure 9. Morphological characterization of one layer printed film without ironing (OLF).	19
Figure 10. Morphological characterization of two layers pressed film.	19
Figure 11. Morphological characterization of one layer printed film with ironing (OLFI).	20
Figure 12. DSC spectra of P(VDF-TrFE) pellet, fibre, TLPF and OLFI.	21
Figure 13. FTIR spectra of P(VDF-TrFE) pellet, fibre, TLPF and OLFI.	21
Figure 14. XRD spectra of P(VDF-TrFE) pellet, fibre, TLPF and OLFI.	22
Figure 15. Studied configuration a) AOA, b) PCOC and c) COC.	23
Figure 16. Curves of capacitance (full line) and loss tangent (dash line) of COC, PCOC and AOA configuration.	24
Figure 17. Curve of a) COC bipolar polarisation, b) COC unipolar polarisation, c) PCOC bipolar polarisation, d) PCOC unipolar polarisation, e) AOA bipolar polarisation and f) AOA unipolar polarisation.	26
Figure 18. Hysteresis cycle of COC configuration at 69 MV m ⁻¹ , PCOC configuration at 62 MV m ⁻¹ and AOA configuration at 39 MV m ⁻¹ .	27
Figure 19. Curve of the pyroelectric response using the generated current and voltage of a) COC configuration, b) PCOC configuration and c) AOA configuration.	28
Figure 20. Measurement of device response with AOA film after polarisation.	29
Figure 21. PVDF and P(VDF-TrFE) molecular structures.	39
Figure 22. Electric circuit for rectification and control of input signal on the amplifier.[70], [71]	42
Figure 23. Electric circuit to the measurement of the sample current during the polarisation.[70], [71]	43
Figure 24. Sample during polarisation in a silicon bath at 90 °C.	44
Figure 25. Sample during the measurement of pyroelectric response.	45
Figure 26. Used setup in capacitance measurements.	46
Figure 27. 3D model device.	47
Figure 28. Testing the device providing an heat source.	48
Figure 29. Testing the device in absence of an heat source.	48
Figure 30. Top surface of sheet resistance samples dried at 155 °C on the hotplate.	49

List of Tables

Table 1. Properties of Solvne®250 EAP from SOLVAY SPECIALTY POLYMERS ITALY S.p.A...	9
Table 2. Resume of sheet resistance characterization.....	16
Table 3. Element quantification of 3D printed electrodes by SEM-EDS.....	18
Table 4. Resume of samples characterization.....	29
Table 5. Additional properties of Solvne®250 EAP from SOLVAY SPECIALTY POLYMERS ITALY S.p.A.....	40
Table 6. Additional properties of Conductive PLA Proto-Pasta from Protoplant.	40
Table 7. CAS Number of used materials.	40
Table 8. Parameters used in Ultimaker Cura 4.0.0.....	41

Motivation and objectives

Nowadays, three-dimensional printing technology is one of the fastest-growing technologies. Deloitte predicts that the market related to this sector, which has a revenue of around US\$12 trillion annually, will surpass US\$2.7 billion in the current year and US\$3 billion in 2020.[1]

The inevitable interest in this technology is linked to its concept which is attractive to the industry, academia and also the domestic consumer. The possibility of applications offered by 3D printing is huge. Its characteristic features are the design of a specific object, the wide range of materials which can be used due to the huge development around the technique and supplies, the low production costs and the most important one is the effortless design.[2]

The possibility of using new materials in 3D printing open new opportunities in the energy area like energy harvesting. Nowadays, energy harvesting is a common subject due to the necessity of developing other ways to produce “clean” energy, to ensure enough ways of fighting a possible energy crisis in the coming decades. Furthermore, energy harvesting is a smart way to obtain energy from wasted energy sources, using for example piezoelectric materials to generate energy with human motion. In the last decades, energy harvesting had some challenges about the durability, portability and flexibility of the produced devices. These challenges were solved with the discovery of great piezoelectric properties of some polymers, like poly(vinylidene fluoride-trifluoroethylene) (P(VDF-TrFE)), a copolymer of polyvinylidene fluoride (PVDF).[3]

Seeing the emergence of the 3D printing process and the possibility of using functional polymers to produce energy harvesting devices, with great mechanical properties inherent to polymers, the interest in combining them result in this work. The focus of this work will be the production and study of P(VDF-TrFE) films via 3D printing. Before the production of the films, the main focus was the production of filament and optimization to be used in a 3D printer. Another objective of this work is the full production of a sensor based on P(VDF-TrFE) film with printed commercial conductive polylactic acid electrodes. As it will be demonstrated, it was also produced a sensor with evaporated aluminium electrodes. By optimizing the printing and polling process it was possible to obtain an uniform thin film and a reasonable electric response.

Work Strategy

The present work was split into five main stages:

1. Production and optimization of electrodes using a 3D printing process with commercial filaments in order to achieve the best mechanical and electrical properties.
2. Extrusion of P(VDF-TrFE) filament.
3. Production and optimization P(VDF-TrFE) films using 3D printing.
4. Polarisation and electric/electroactive characterization of films.
5. Printing and characterization of a full working device.

Chapter I. Introduction

1. Fused deposition modelling

Fused Deposition Modelling (FDM), also known as Fused Filament Fabrication (FFF), is one of the most popular three dimensional printing (3DP) techniques used nowadays. It belongs to a group of fabrication techniques called Additive Manufacturing (AM) which consists of using a CAD file to fabricate an object layer by layer.[4], [5] Scanning, sharing and fabrication of physical object converted from a digital file is only possible with the AM technology.[5], [6]

Recently, the development of the additive manufacturing techniques have increased and let them be used in several industry segments such as automotive, aircraft, electronic and biomedical fields.[5], [7]–[11]

1.1. Working principle of FDM

FDM is based on the hot-melt extrusion, where the filament feedstock, usually with 1.75 mm or 2.85 mm of diameter, is guided through a drive gear mechanism to the liquefier, as shown in Figure 1. The drive gear mechanism is connected to a motor to provide the filament movement. In the heated liquefier, the filament is melted at a temperature above the material melting point. Until the end of printing, the motor is working and the solid filament outside the liquefier will push the melted material through the print nozzle and when the material reaches the substrate, it cools down and hardens.[4], [6], [12] There are two main types of FDM 3D printer regarding the way of axis movement during the printing. In one of them, the platform moves down in z-axis and the print head moves in the x-y plane. In the other type, the platform moves along the y-axis and x-axis while the print head moves side-to-side along the z-axis.[4]

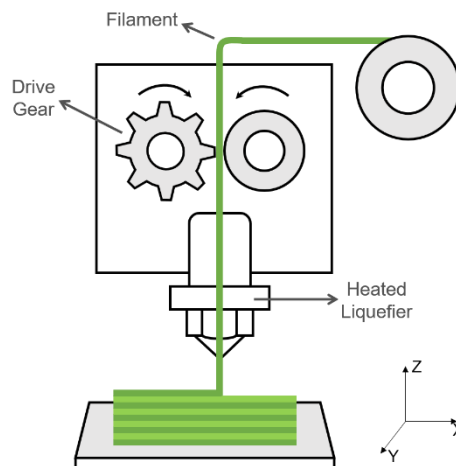


Figure 1. Schematic diagram of the FDM process based on [4].

The technology of FDM process is still growing and showing new capabilities related to the improvements in process optimization and also in the usage of materials which can provide new capabilities to the printed object. The development of this technology advanced due to the reduction of costs on the improvement of this kind of procedures.[4], [12]

1.2. FDM vs Traditional manufacturing techniques

The objects produced by FDM have some limitations and disadvantages when compared with

conventional methods as compression or injection moulded. With FDM the obtained mechanical properties are worse than the usual traditional techniques due to the pore creation in the printing process and the delamination. These can be related to fluctuations in the temperature layers, while in conventional methods are no visible voids.[13]–[15]

The mechanical properties can be affected by the chosen build direction during the printing, being the perpendicular orientation to the built axes the weakest one.[14]

Another issue that FDM process has is related to the biocompatibility of conventional thermoplastic polymers used like ABS (acrylonitrile butadiene styrene) for medical implants or drug delivery devices. There are studies about toxicity of styrene present in ABS worried experts who predict that it may cause cancer in humans when is submitted to long-term contact with the human body. [4], [16] The biocompatibility was studied in other materials like polylactic acid (PLA) which has shown that is nontoxic *in vitro* and *in vivo*, an important characteristic to be used in biomaterial applications without risks for human health.[17]

Another limitation of FDM is the resolution which needs to be improved; even with the increase of expectations about AM technology prototyping quality, this is a major factor while producing new components.[18]

The last drawback of FDM over traditional methods is the limitation of production speed and consequently the limitation in mass production. This drawback only exists when we are discussing large scale production vs in small scales the FDM process, because small scale allows the production of an object without need expensive tools that injection or compression moulding need.

The fused deposition modelling have other advantages over conventional methods such as: capability to increase the object complexity without compromising production, multi-material fabrication, low-cost equipment, does not need a specialized operator, quick production of prototypes, global scale production just by sharing the design file which have all information and parameters that allows the production of same object to everyone. It is also a “green” process due to its layer by layer process which uses an exactly quantity of material to produce the object having a waste reduction. The FDM also enables the use of composites filaments produced to improved electrical or mechanical properties or improve biocompatibility, adding certain materials to a polymeric matrix.[4], [6], [18], [19]

2. Extrusion fundamentals

Extrusion is a great method to produce fibres because it converts raw material into a product of uniform shape and density by forcing it through die under controlled conditions.[20] An extruder is divided into two parts: one part transports the material and other shapes the materials into the required form. Temperature is used in this method in order to control the viscosity of the material, enabling it to flow through the die, named molten extrusion. It is also possible to extrude materials using a semisolid system which is a multiphase concentrated dispersion containing a high proportion of solid mixed with a liquid phase.[21]

The extrusion channel is divided into three sections: feed zone, transition zone and metering zone. The material reaches the feed zone directly from the hopper. The geometry of the screw in the feed zone enables the material to fall easily into the screw for conveying along the barrel. After entering the channel, the material is transported to the transition zone, where is mixed, melted and compressed. The

last zone where the material passes inside the channel is the metering zone, where the material arrives like a homogeneous plastic melt suitable for extrusion. This last zone ensures that the flow of material which achieves dye cavity is uniform, to achieve a uniform thickness of produced fibres. The absence of stagnant zones right up to the die entrance is also important to obtain fibres with uniform thickness. [20], [21]

3. Functional materials

Functional materials have the capability to exhibit other functions under a determined stimulus. These materials are classified according to the electric, magnetic and or optical properties associated with the function that material show. One of the most commons functional materials used is electroactive materials including piezoelectric, pyroelectric and ferroelectrics for applications like sensors or actuators. These functionalities are related to the chemical composition, singularities of the crystallographic structure and manufacture process.[22]

3.1. Electroactive polymers

In the group of electroactive materials, the electroactive polymers (EAP) are highly attractive because of the inherent properties of the polymers such as easy to process, good mechanical properties and being lightweight.[23] Beyond the good properties of polymers, the EAP is the most interesting class of polymers because has the possibility to work as an actuator or sensor. These capabilities rely on if it responds mechanically to electrical stimulation (actuator) or responds electrically to a mechanical stimulus (sensor).[24] Furthermore, EAP is also seen with great potential to biomedical applications because of their flexibility and strain response that been compared with human muscles, calling them "artificial muscles". [24], [25]

The electroactive polymers are divided into two main groups: ionic electroactive polymers (IEAP) and electronic or field-activated EAP. The mechanism of activation the ionic EAP involves transport or diffusion of ions [23], while in electronic electroactive polymers (EEAP) an electric field is applied in films of polymeric material producing Coulomb forces which orientate de dipoles of material. [23] Comparing IEAP with EEAP, the main advantage is the use of lower activation fields. However, the second one offers more advantages such as fast response, greater mechanical energy density, the capability to be activated in air and do not have the problem of maintaining the material wetness, which the ionic EAP has, and do not require encapsulation in order to operate in open-air conditions.

After comparing both groups of EAP it can be easily concluded that the electronic EAP has better properties if the intensity of the used electric field is not taken into account. [23], [25] Electrostrictive polymers, dielectric elastomers, liquid-crystal elastomers and ferroelectric materials are the four main subgroups included in the electronic type of EAP.[26], [27] In these main subgroups, the ferroelectric materials received more attention since, in 1969, Kawai[28] observed a substantial piezoelectric activity which can be permanently induced in stretched polyvinylidene fluoride (PVDF). This was followed by the discovery of the pyroelectricity of the same polymer two years later with the work of Bergam et al.[29] leading to a growing interest in the study of ferroelectric polymers until today, in special the PVDF and is copolymer poly(vinylidene fluoride-co-trifluoroethylene) (P(VDF-TrFE)).[23]–[25]

3.2. Ferroelectric, pyroelectric and piezoelectric materials

Ferroelectrics are materials that exhibit spontaneous electric polarization which is reversible with the application of an electric field.[30] Ferroelectric materials have two phases related to the Curie temperature (T_c), being in the paraelectric phase at temperatures above T_c where the spontaneous polarization is lost, while below T_c the material is in the ferroelectric phase and is composed by spontaneous aligned dipoles.[30] In Figure 2 (a) is observed the spontaneous or reversible polarisation and the transition temperature of ferroelectrics by the peak of the curve. These materials are also characterized by the ferroelectric hysteresis, shown in Figure 2 (b), usually with a broad rectangular shape with polarisation based on the applied electrical field.[30]

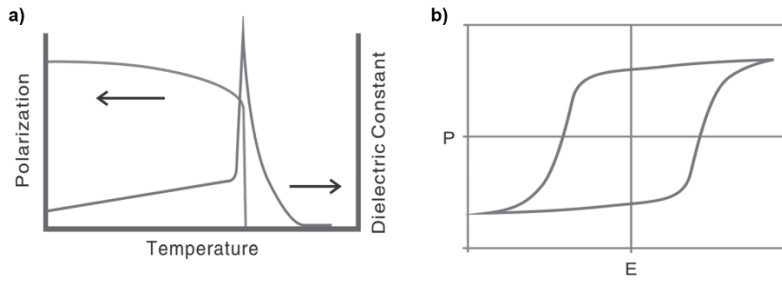


Figure 2. Ferroelectric a) phase transition of ferroelectric to paraelectric b) polarization hysteresis from [30].

Piezoelectricity is the ability of some materials to generate electrical charges in response to mechanical stress (direct effect). The material is also called piezoelectric if a mechanical deformation results when is applied an electrical potential (converse effect).[22], [26]

Pyroelectricity is based on the change of spontaneous polarisation with the change of temperature. The performance of pyroelectric materials is characterized by the pyroelectric coefficient (p_i) that relates the generated current (i_p), the area (A) and the change of temperature (ΔT) in a period of time (Δt), as shown in equation 1.[31]–[33]

$$p_i = \frac{i_p \cdot \Delta t}{A \cdot \Delta T} \quad (1)$$

To provide a better comparison between two different materials it was calculated the figure of merit (FOM). Usually, the FOM is used in sensors with a voltage read-out circuit to evaluate pyroelectric materials. The FOM is also defined as F_v and can be calculated by equation 2.[34]

$$F_v = \frac{p_i}{\epsilon_r} \quad (2)$$

To calculate the F_v it was required the relative permittivity which can be obtained from equation 3.

$$\epsilon_r = \frac{C \cdot d}{\epsilon_0 \cdot A} \quad (3)$$

3.3. Ferroelectric polymers

The science of ferroelectric polymers has been boosted by the discover of PVDF and its copolymers capabilities as ferroelectric material. The study and development of those materials were carried on by the interest in advanced energy technologies and new applications such as flexible sensors [35]–[38], organic-based field-effect transistors[39] and energy generators for energy harvesting.[40], [41] The ferroelectric materials were substituting the traditional ceramics used for years.[30]

PVDF has the chemical formula of $(-\text{CH}_2-\text{CF}_2-)_n$, shown in section A of appendices, but could have different molecular and crystal structures, which depends on the processing conditions of the material.[42] According to different chain conformations, this semicrystalline polymer exhibits five different crystalline phases: *all-trans* (TTT) planar zigzag for the β phase, TG^+TG^- (*trans-gauche-trans-gauche*) for the α and δ phases, and $\text{TTTG}^+\text{TTTG}^-$ for γ and ϵ phases.[30]

The strong electrical dipole moment of the PVDF monomer unit ($5-8 \times 10^{-30}$ C m) is important for sensor or actuators applications devices, achieving the highest dipolar moment in the β phase. [42] There is also in the β phase that was reported the largest piezoelectric coefficient of -34 pC N $^{-1}$, having the larger value when compared with any other polymer. The γ and δ phases also contribute to the overall dipolar moment of monomer unit.[42] By other hand, the α and ϵ phases are macroscopically non-polar due to the self-cancellation of the dipolar moments between the two antiparallel chains within the unit cell.[30], [42], [43] The transformation of α on β phase is the most common way to obtain a maximum quantity of β phase. To achieve this maximum transformation there are some strategies obtained by submitting the sample to an electric field under a mechanical stretching of the sample and at a controlled temperature. The addition of fillers which will act as nucleating agents of the electroactive phase is also used. [42]–[44]

The P(VDF-TrFE) with molecular formula $(-\text{CH}_2-\text{CF}_2-)_x(-\text{CFH}-\text{CF}_2-)_y$, shown in section A of appendices, also creates a great interest in the scientific community for being a PVDF with better ferroelectric properties.[45] The best properties that copolymer show are related with the introduction of trifluoroethylene (TrFE) comonomer between 20 % and 50 % into vinylidene fluoride (VDF), affecting the crystallization of material in β phase.[42], [43], [46] This copolymer is an important example of the influence which molecular defects can have in the intermolecular interactions and consequently in the physical properties of the polymer.[47], [48] P(VDF-TrFE) could be synthesized through the free radical polymerization of the two monomers.[47]–[49] The steric and electronic repulsion between $(-\text{CFH}-)$ of TrFE and $(-\text{CF}_2-)$ in VDF makes that the copolymer has a larger interchain distance when compared with PVDF homopolymer.[50] The increases of interchain distance result in a weaker interchain interaction which will directly affect the Curie temperature. Weaker interchain interactions will reduce the T_c of the copolymer and approximate to the melting point of the polymer, with the objective of crystallizing the polymer at the closest temperature of ferroelectric to paraelectric transition. [51]–[53] In general, PVDF and P(VDF-TrFE) have similar properties, except the piezoelectric coefficients d_{33} and k_{33} which are larger in the copolymer.[54]

4. Fused deposition modelling of ferroelectric polymers

The first attempts using piezoelectric materials via FDM using PVDF were performed by Kim et al.[55] while trying to obtain better piezoelectric properties adding BaTiO₃ (BTO) nanoparticles about 100 nm in PVDF matrix. In their work, it was prepared a solution of PVDF and BTO (9 wt.%) to produce films via solvent-casting. These produced films were cut to feed an extruder to create a filament to be used in FDM equipment and to print PVDF/BTO films in the 3D printer. Both films, solvent-casting and 3D printed, were submitted to thermal polling at 90 °C for 2h, with an electric field of 35 MV m $^{-1}$. At the end of this study, the results have shown that 3D printed films have a better piezoelectric response with higher output current which was explained by the homogeneous dispersion and the reduction of

agglomerates of BTO particles.[55]

In Lee et al.[56] work it was used a procedure to combine polling and FDM to create a new method called electric polling assisted additive manufacturing (EPAM). The modification of the conventional FDM process was the application of an electric field between the nozzle and the print bed of machine, covering the print bed with kapton tape to electrical and thermal insulation. During the printing process, the applied electric field will promote a dipole alignment while the PVDF is molten, being easier to align the dipoles using lower voltage because dipoles have better mobility. It was applied 1 MV m^{-1} and 2 MV m^{-1} on films, obtaining higher currents in the films where was applied the highest electric field and which was also related to a larger presence of phase β in FTIR analysis.[56]

Kim et al. [57] tried a new approach using an EPAM similar process to printing the same films of PVDF/BTO some years after their initial work about 3D printing films of PVDF/BTO. In this new method it was added glass, steel plate (cathode), kapton tape and masking tape over the print bed to prevent the electrical breakdown due to the higher electric fields in use. In this study, the interest in the increase of the applied electric fields is related to the limitation of the EPAM process in printing and polarization of only one layer. Changing this process made possible the printing of multilayers without achieving the breakdown or damage the 3D printer.[57]

In a similar work, Kim et al.[58] studied the PVDF films printed via FDM with some modifications, using the same layers over the print bed (glass, steel plate, kapton tape and masking tape) with the same purpose. These films of PVDF were printed and afterwards the hot nozzle was moved over the printed layer applying a higher electric field in order to orientate the dipoles of the polymer. This work was based in corona polling which does not need contact between the nozzle and the sample, creating a charge layer on the surface of the sample, by the ionization of the air.[58]

Marandi et al.[59] compare PVDF with the copolymer (P(VDF-TrFE) using corona polling to orientate the dipoles of the polymer. They produce two types of samples: single-layer sample and double-layer sample. The single-layer sample was only printed via FDM process and polled. The double-layer sample was composed by one layer of P(VDF-TrFE) as an electroactive layer, an electrode made with conductive paint and a non-electroactive layer of PVDF which work as a substrate and a protective layer. In their work, this PVDF layer introduces larger stress in the electroactive layer which increases the piezoelectric response of the samples. In this study is also seen by XRD spectroscopy that the copolymer has more emergence of β phase than the PVDF. It was observed an electric response of 0.65 V for single-layer sample and a signal of up to 130 V peak to peak for double-layer. These results confirm the great piezoelectric properties of this material. [59]

Chapter II. Materials and Methods

1. Materials

For additional information about all the used materials consult section B of appendices.

1.1. P(VDF-TrFE)

The P(VDF-TrFE) copolymer used was the Solvене®250 EAP from SOLVAY SPECIALTY POLYMERS ITALY S.p.A. This polymer has a molar content ratio of 75/25 and has interesting properties, shown in Table 1, that are good for produce sensors or actuators. It has been used the copolymer instead of PVDF because the β -phase is usually created in transition melt-solid of polymer while in PVDF the majority of the polymer goes to α -phase.[59] The original form of this electroactive polymer was pellet based which were then transformed in fibres and then in thin films.

Table 1. Properties of Solvене®250 EAP from SOLVAY SPECIALTY POLYMERS ITALY S.p.A..

Properties	Solvене®250 EAP	Unit
Melting temperature	146	°C
Curie temperature	116	°C
d_{33}^* (measured by Berlincourt method at 110 Hz)	-24	pC N ⁻¹
Coercive field	65	V μm^{-1}
ϵ_r (25 °C, 1 MHz)	11	

*Values obtained poling at 200 V μm^{-1} , 25 μm thick film printed PEDOT:PSS electrodes.

1.2. Conductive PLA Proto-Pasta

Some electrodes were printed using a conductive PLA Proto-Pasta (CPLA) from Protoplant. This material is provided in filament and is a compound made of Natureworks 4043D Polylactide (PLA) and conductive carbon black. This provides better electrical properties to the filament represented with the resistance to a length of 10 cm filament and 1.75 mm diameter of 1.8 k Ω and a volume resistivity of 3D printed parts through layers (along the Z-axis) of 115 $\Omega \text{ cm}^{-1}$.

2. Sample production

2.1. Fibre extrusion and filament production

To extrude the filament of Solvене® 250 EAP it was used the Xplore MC5 micro compounder. The extruding has been done at 150 °C, with a nozzle of 1.3 mm and feeding the extruder about 4.5 g of pellets of P(VDF-TrFE) to obtain fibres with 1.75 mm of diameter and length of 1 m.

The extruder has two working modes: speed mode and force mode. The speed mode has been used during the feeding of material and is controlled by the rotating speed of the screws, using a speed of 100 rpm and a maximum force of 3 kN. During the extruding of the fibre, was used the force mode to increase the uniformity of the fibre diameter, using a maximum speed of 300 rpm and a force between 1.4 kN and 1.7 kN, varying to obtain a speed around 28 rpm which also increase the uniformity throughout the fibre.

The extruder only can be fed with a maximum of 5 g each time, which limits the length of the filament to a maximum around 1 meter. To feed the 3D printer it is required a long filament, so it has been used a piece of brass with a groove with a diameter of 1.75 mm which has been heated around 170 °C to merge the extruder fibres to each other.

2.2. 3D Printing of P(VDF-TrFE) film

In the design of the P(VDF-TrFE) film it was used Autodesk Fusion 360, drawing a film with a square shape with 15 mm side and 0.03 mm of height. After the design of the films it was used Ultimaker Cura 4.0.0 to choose the specific parameters of the 3D printing for Creality Ender-3. Some of these parameters were the print speed, layer height, infill density and even the thickness of the wall that is very important in the quality of films with just a few layers of material. In section C of appendices there is more information about the parameters used in the printing of P(VDF-TrFE) films.

The production of samples in 3D printer ends with the printing of the design pieces in Creality Ender-3, using a bed printer of glass at 60 °C and a nozzle of 0.4 mm at 200 °C. Before the printing, the printer has been calibrated and it was used a hair spray in bed printer to enhance the adhesion of the first layer to the stage.

Only one layer is printed during the printing of P(VDF-TrFE) films to obtain the minimum thickness of this film. To enhance the quality of the surface was used a feature of 3D printer called ironing. This process consists in a second layer where the nozzle does not extrude any material but stay at 200 °C and smooth the surface when passing over the printing layer.

2.3. 3D Printing of conductive PLA Proto-Pasta samples to study sheet resistance

The sheet resistance of CPLA was studied to understand how it could obtain electrodes with the best electrical properties. To study the sheet resistance of conductive PLA Proto-Pasta it was designed and printed samples using the same process used in P(VDF-TrFE) films but with 15 mm × 20 mm and up to five layers, each layer with 0.03 mm of height and without using the ironing feature. In a second step, the samples were covered at the ends along the longer axis with water-based silver conductive ink (PE-WB-1078) from Conductive Compounds to create electrodes. Half of the samples were dried at room temperature and the other was dried 3 min at 155 °C on a hotplate. This difference in the drying process was performed to study if there is a significant influence on the conductivity of the material related to different temperatures. Lastly, it was measured the resistance between electrodes made of silver conductive ink with a multimeter and it was calculated the sheet resistance for samples with a different number of layers and with variations on the drying process.

2.4. 3D Printing of conductive PLA Proto-Pasta electrodes

The design of electrodes was also done in Autodesk Fusion 360 where electrodes were defined as circles with 10 mm of diameter and 0.12 mm of height using conductive PLA Proto-Pasta. To choose the printing parameters it was used the same way of films but using a smaller wall thickness which is related to the shape of the electrode. In these electrodes it was not used ironing because the difference was not significant and does not compensate the increase of printing time. In section C of appendices is more information about the parameters used in the printing of CPLA electrodes.

2.5. Evaporation of aluminium electrodes in P(VDF-TrFE) film

To obtain electrodes it was deposited aluminium (Al) in P(VDF-TrFE) film by evaporation using masks of circles with 10 mm of diameter. The deposition of 85 nm of Al was made on both sides of the film in order to prepare the sample to the step of polarization, with a current around 55 A and a deposition rate around 0.5 nm s⁻¹.

3. Sample characterization

3.1. Structural, chemical and morphological characterization

During the production of the samples, the materials were tested in different states, since from the pellets of Solvne® 250 until the films and conductive PLA Proto-Pasta. To understand if there are differences in the physical properties of the material it was made Differential Scanning Calorimetry (DSC) with the Simultaneous Thermal Analyser STA 449 F3 Jupiter to pellets, fibre and films of P(VDF-TrFE) from 20 °C to 270 °C with a step of 10 °C/min.

The same samples were also structurally characterized with X-Ray Diffraction (XRD) using the PANalytical X'pert PRO MRD with a monochromatic Cu-K α (wavelength 1.5406 Å) radiation source, applying 40 mA of current and 45 kV of voltage, with a 2 θ range between 10° and 60°. To obtain a better characterization of the possible changes in the different stages of the material it was done an analysis on Fourier-Transform Infrared Spectroscopy (FTIR) using Thermo Nicolet 6700 with a wavelength between 525 cm⁻¹ and 4500 cm⁻¹ with a 4 cm⁻¹ resolution.

To verify the composition of the conductive PLA Proto-Pasta it was made a chemical analysis to a printed round electrode with Scanning Electron Microscopy (SEM) Hitachi TM3030Plus tabletop workstation using Energy Dispersive Spectroscopy (EDS).

Finally, it was used the Optical Microscope Olympus BX51 to see the morphology of all samples (P(VDF-TrFE) film, the round electrode of CPLA and the samples used to study the sheet resistance) to compare the top and bottom surfaces of each sample. In the case of samples used for the study of sheet resistance it was theorized if it could be helpful to understand the differences in electrical properties between them.

4. Electrical characterization

4.1. Polarisation

The electrical characterization started with the samples polarisation using a setup composed by a 100 MHz TGA12104 arbitrary waveform generator from Aim-TTi, a TREK MODEL 610E amplifier, a TDS 2001C oscilloscope from Tektronix and equipment to rectify the signal. The signal rectification was done in zone 1 of Figure 3, based on the electric circuit presented in section D of appendices. It was also used a circuit based on the scheme displayed in section E of appendices which could be simplified with an Op Amps TL082 with a 50 k Ω resistance, shown in zone 2 of Figure 3.

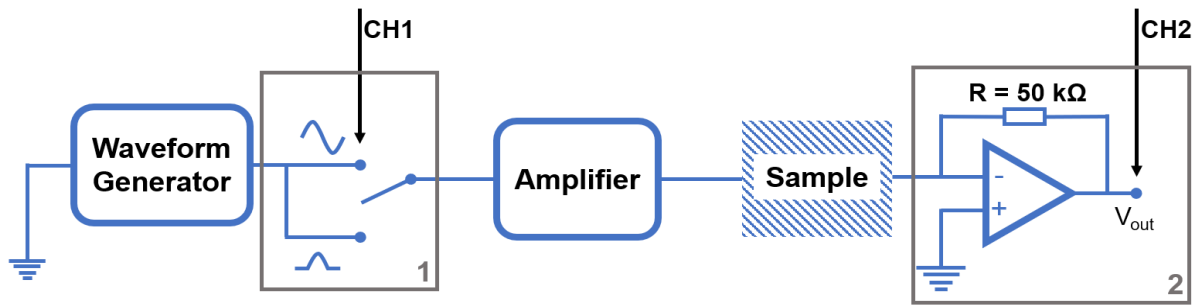


Figure 3. Used setup in samples polarisation.

The applied electric field was increased until evidence of polarization was observed. The amplifier can amplify 100 or 1000 times the signal that came from the waveform generator, which previously passes for the rectify equipment to define what signal will achieve the sample.

After seeing an evidence of polarisation, the sinusoidal signal is rectified to a half signal. The rectification it was done to retain the polarisation in the sample. To align the dipoles in one orientation is primordial the use of unipolar signal because by using a bipolar sinusoidal signal the dipoles will always change their orientation. Finally, the oscilloscope usage is measured by the generated signal before the amplification and the output voltage (V_{out}), which is important to calculate the current which passes the sample. Beyond the V_{out} is crucial known the value of the resistance in zone 2, because without that value is not possible to obtain the current by Ohm's Law.

The polarisation is easily achieved using mid temperatures because the material is softened and the dipoles gain larger mobility which enables the alignment of dipoles with lower electric fields. The best way to obtain a homogenous temperature of the sample during the polling process is by using a silicone bath at 90 °C, heated with a hotplate. In section F of appendices is presented a sample during the polarisation.

4.2. Measurement of pyroelectric properties

In order to characterize the samples after polarisation it is used a setup with a TGA12104 arbitrary waveform generator 100 MHz from Aim-TTi, a power supply, a 617 programmable electrometer from Keithley Instruments, a temperature sensor, a peltier and an Arduino controller, shown in Figure 4.

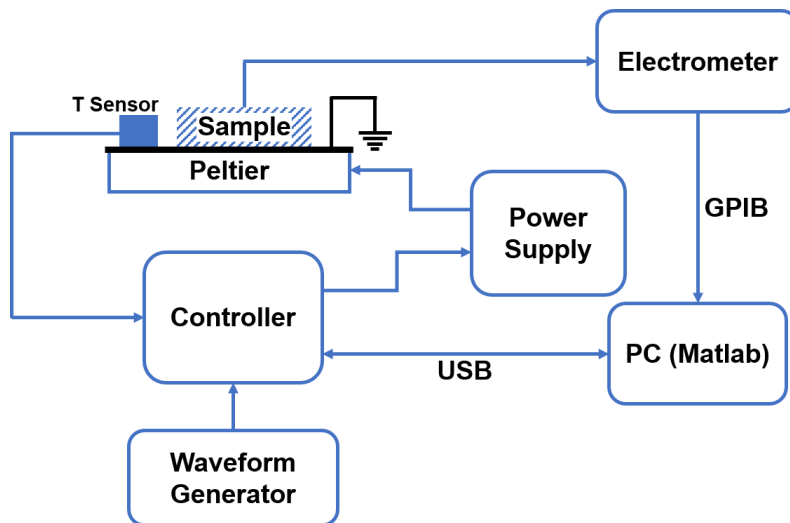


Figure 4. Used setup in measurements of pyroelectric properties of samples.

The working principle of the previous setup is based on the variation of the temperature and measurements of currents and voltages that are generated by the electroactive film at the same time. The waveform generator is used to control the variation of the temperature using the offset parameter to set the average temperature and the applied voltage to define how much the temperature varies around the temperature set by offset. In these measurements is used an offset of 1.8 V, a voltage peak-to-peak of 2.5 V and a frequency of 0.1 Hz. The variation of the temperature of peltier is controlled by the power supply which is consequently controlled by the controller. At the same time, this variation is measured by a temperature sensor which is connected to the controller which sends that information to the computer (PC). While the peltier is working, the sample is heated and generates a current or voltage which is measured by the electrometer that sends the values to the PC using a GPIB connection. In the computer is used a script in Matlab that plots the received values of temperature and current or voltage versus time. In Figure 25 of section G of appendices is presented a sample during the measurements of pyroelectric responses.

4.3. Measurement of capacitance

The measurement of the capacitance of the samples is performed by inserting films between two plates, as shown in section H of appendices, which are connected to the 4294A Precision Impedance Analyzer from Agilent to obtain the results.

5. Device production and experiments

The device is designed in Autodesk Fusion 360, shown in section I of appendices, and printed in the 3D printer used for the production of the films. It was projected to put the sample between the two pieces which have printed conductive tracks using CPLA and using commercial PLA to give structural basis to this full printable pyroelectric sensor.

This device is done to prove that the produced and polarised films have good properties to use them in a sensor. It was measured the signal when the sample is submitted to the radiation of a simple halogen lamp to confirm the capabilities of the produced structures, using the simple setup presented in section J of appendices.

Chapter III. Results and Discussion

This chapter begins with an electrical and morphological characterization of the printed electrodes and is also performed a study about the sheet resistance of them. The next step in this work is a discussion on P(VDF-TrFE) films, studying the influence of processes during the production of the films, since pellets shape to film, to obtain the maximum information about the material. The work ends with the characterization of the films in order to obtain information about the influence of the applied electric fields and used electrodes in the polarisation. The ferroelectric properties of the material were also studied to understand the possibility of implementing it on a pyroelectric device.

1. Conductive PLA characterization

1.1. Study of sheet resistance

The characterization of conductive PLA begins with studying the influence of the number of layers in the sheet resistance (R_{sh}) of the CPLA. There were used 20 samples in this study, changing the number of layers between 1 and 5 (in batches of 4 samples each one). Silver conductive ink was used to create the electrodes in the samples. Half of the samples were dried at room temperature (RT) and the remaining samples were dried 3 min at 155 °C on a hotplate (HP). This division ensured that two samples submitted with the exact same parameters (number of layers and dry process) were used to obtain a better precision in the results. The resistance (R) measured according to equation 4 with a multimeter between the electrodes was used to calculate the sheet resistance using equation 5, where ρ is the resistivity, t is the thickness of the sample, L the distance between electrodes and W the perpendicular distance to L . [60]

$$R = \rho \cdot \frac{L}{W \cdot t} = \frac{\rho}{t} \cdot \frac{L}{W} \quad (4)$$

The ratio between resistivity and thickness is named sheet resistance, which results in the Ω/\square unit. [60]

$$R_{sh} = \frac{R \cdot W}{L} \quad (5)$$

The relationship between the number of layers and the obtained sheet resistance was exposed in Figure 5.

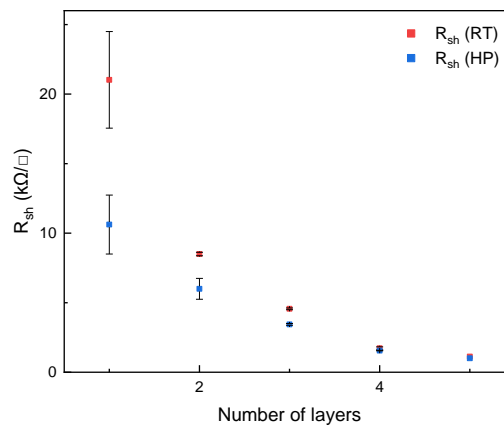


Figure 5. Study of sheet resistance with the increasing of the number of layers and comparison between the room temperature dry process of silver conductive ink electrodes with dry of 3 min in hotplate at 155 °C.

With the analysis of Figure 5 it has been clearly seen a decrease in the sheet resistance with the increasing number of layers. This was expected due to the inverse proportionality between the sheet resistance and thickness. In Table 2 is presented the values of the sheet resistance of each sample with different number of layers, for samples dried at room temperature and on a hotplate.

Table 2. Resume of sheet resistance characterization.

Number of layers	R_{sh} (RT samples)	R_{sh} (HP samples)
1	21.03 ± 3.48	10.62 ± 2.12
2	8.50 ± 0.13	6.00 ± 0.75
3	4.56 ± 0.06	3.44 ± 0.06
4	1.72 ± 0.11	1.56 ± 0.02
5	1.13 ± 0	1 ± 0

Beyond the inverse proportionality, the R_{sh} tends to stabilize at $1 \text{ k}\Omega/\square$ in both dry processes. Comparing the samples with the same number of layers but submitted to different dry processes is easily observed that samples dried in a hotplate have lower sheet resistances than samples dried at room temperature. This difference could be related to a promoted annealing of the samples during the drying process which will turn the surface into a more homogenous one.

It is also denoted a decrease in the stiffness of the samples with the increasing of the number of layers and a difference between the first printed layer (bottom surface) and the last printed layer (top layer).

Sample surfaces with a different number of layers were observed using an optical microscope, in order to study the annealing influence of the samples as well their morphological characteristics. The top and bottom surfaces of samples at room temperature and the bottom surface of samples dried on a hotplate were compared in Figure 6. To see the images of the top surface of samples dried on hotplate go to section K of appendices.

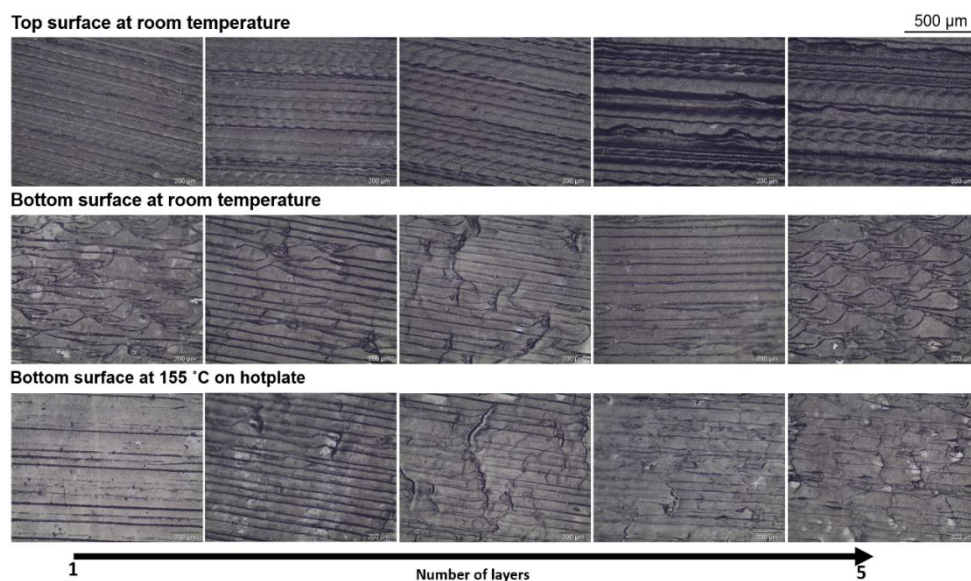


Figure 6. Morphological images of the top and bottom layers surfaces of used sheet resistance samples, with a different number of layers and different dry processes.

The analysis of the morphology of the samples was done in two parts: comparison between the top and bottom surface of the same sample and between the same surface of different samples. Beginning with an analysis of the same sample is observed that the bottom surfaces (BS) have a more homogenous surface comparing with the top surface (TS). When analysing the influence of the different number of layers have in the surfaces is easily observed that there is an increase of irregularities on the top surface with the increase of layers. This is justified by the lower resolution of printing process, where the irregularities are propagated layer by layer due to the new layers being printed over layers that are already irregular.

The influence of increasing the number of printing layers is visible in the BS with the increasing of cracks and flaws, which is an explanation of the decreasing of the stiffness observed previously. The origin of these defects is related to the degradation of the material caused by the longer exposure of printing layers to the nozzle at higher temperatures during the printing of new layers. It was observed more defects on the samples with more layers.

The morphological analysis ends with the comparison between the surface of samples dried at room temperature and on a hotplate. It was only compared the bottom surfaces because they are the surfaces that show more significant differences. These differences are more visible in bottom surfaces due to the samples being placed with the bottom part in contact with a hotplate and with reduced time of exposure the sample could not heat homogeneously. The HP samples show fewer and smaller defects comparing with RT samples with the same number of layers. These can be justified by the softening of the samples which lead to homogeneity of the surface resulting in lower sheet resistance of heated samples.

It was concluded that the best option is producing a 3D printed electrode with 4 layers by comparing the obtained results of sheet resistance and morphological analysis. This use case achieved one of the best sheet resistances and at the same time a considerable mechanical resistance due to the absence of critical cracks in the surfaces. The electrodes were not heated for posterior steps, because with this number of layers the difference in sheet resistance is not significant, which could reduce the complexity of the process eliminating this step.

1.2. Characterization of 3D printed electrodes

It was performed a morphological analysis to printed electrodes, as shown in Figure 7, expecting similar characteristics to the samples used to calculate the sheet resistance.

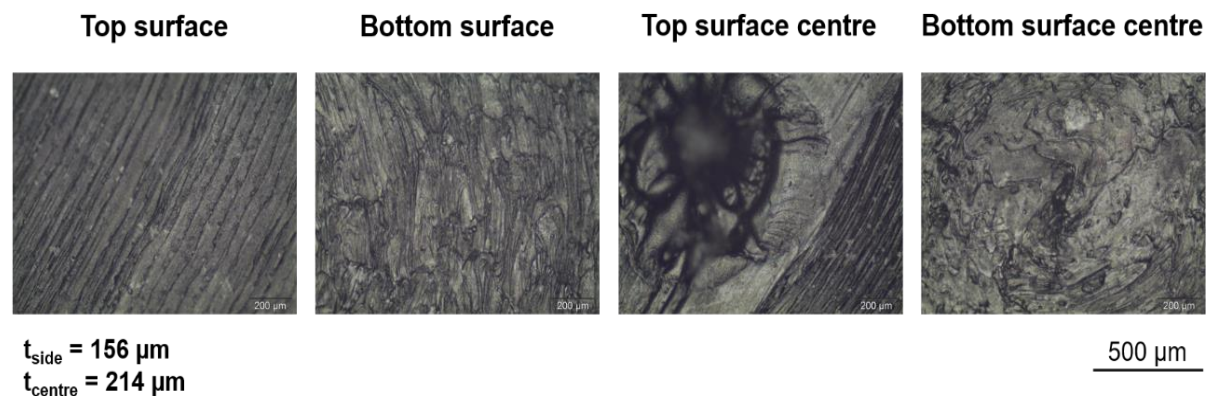


Figure 7. Morphological characterization of the 3D printed electrode.

With images obtained with an optical microscope it is possible to observe that the top and bottom

surfaces in the side of this sample as well the previous samples have a similar irregularity. However, in this sample it was also seen a changing in the thickness between the sides and the centre of the sample. This was caused by the 3D printing process at the end of the printing process which left a small peak of material in this location. This variation in the thickness is not significant in the working of this sample, making unnecessary the use of ironing in this samples in order to spare time in all printing process.

To confirm the composition of the used material it is performed an SEM-EDS analysis presented in Table 3 and Figure 8.

Table 3. Element quantification of 3D printed electrodes by SEM-EDS.

Element	Zone 1		Zone 2		Zone 3	
	wt. %	at. %	wt. %	at. %	wt. %	at. %
Carbon	69.32	80.49	79.03	83.47	80.81	84.87
Oxygen	15.55	13.56	20.75	16.45	19.19	15.13
Chlorine	15.13	5.95	0.23	0.08	-	-

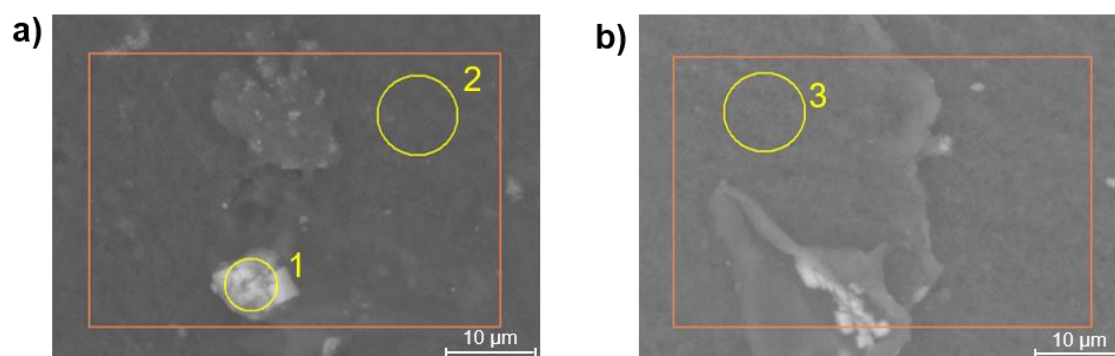


Figure 8. SEM-EDS of 3D printed electrodes of a) top surface, and b) bottom surface.

Analysing simultaneously the previous table and figure it is easily concluded that the material corresponds to the expected conductive PLA, composed by PLA and carbon black. This is possible to conclude by the huge quantity of carbon in both analysed zones and surfaces. In the zones 1 and 2 there is present chlorine, especially in the zone 1 which have high quantity in a particle that is considered a contamination which can be related to the use of hair spray in the printing process of the samples. At the same time it is not found significant quantities of chlorine and the shape is singular and not shows repeatability, as can be observed in Figure 8 (a).

2. P(VDF-TrFE) characterization

2.1. Morphological characterizations of films

In this work, there were produced three types of P(VDF-TrFE) films with the main objective of understanding which is the best option to polarize and turn the production an easier and faster process. The first produced film is a one layer film (OLF) which has a top surface too much irregular for the required application and has a huge difference between the thickness over the sample. This variation in the thickness, shown in Figure 9, is not great to obtain a uniform polarisation of the sample. That can be a problem in the process because of the requirement to use higher electric fields in some thicker

zones with 166 μm which causes disruption of the sample in the thinner zones with 85 μm .

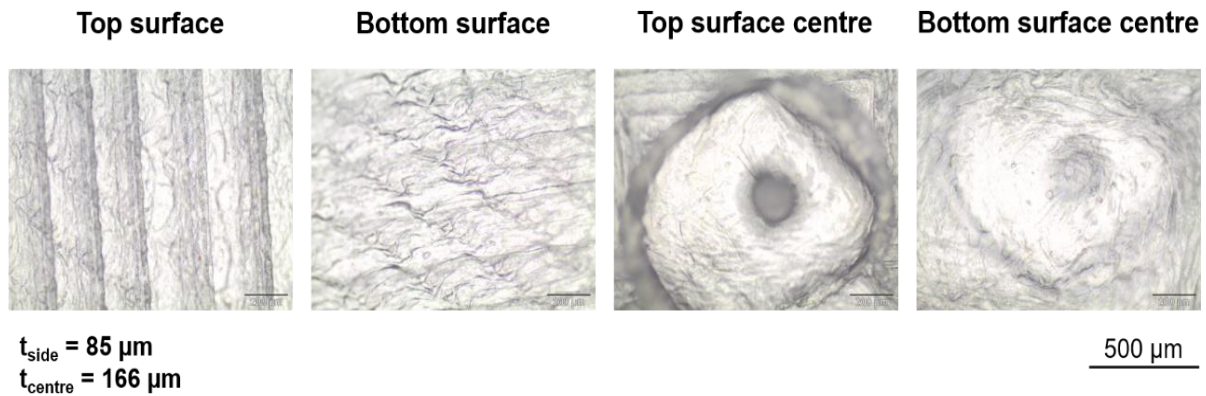


Figure 9. Morphological characterization of one layer printed film without ironing (OLF).

It was found a way to transform this same sample in one of uniform thickness and also decrease the irregularities in the surfaces in order to solve this problem of poor uniformity of the thickness along the sample surface. This was resolved by pressing two of the previous samples with both top surfaces against each other. The pressing process was done 3 min at 140 °C to soften the material and increase the adhesion of both films. Figure 10 shows the morphology of the surface of these two layers pressed film (TLPF), showing a more homogenous surface and without significant variations in sample thickness.

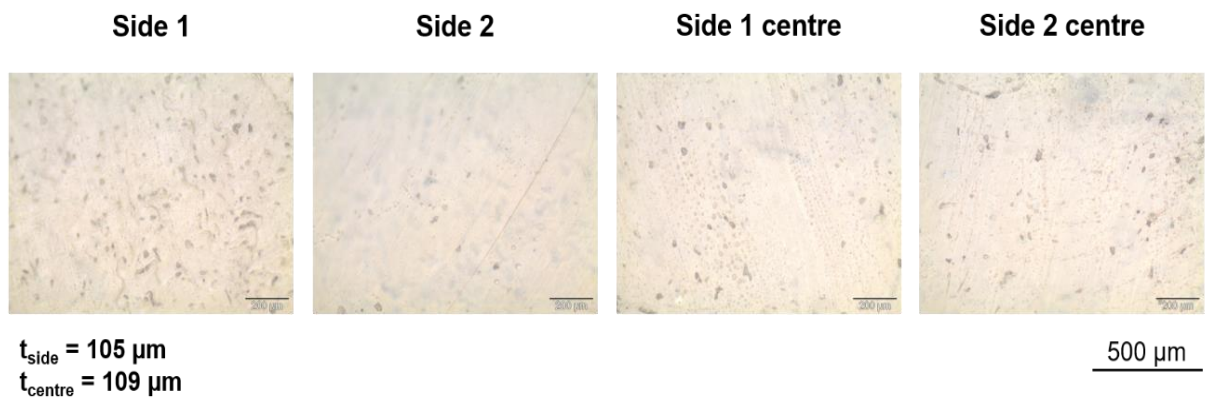


Figure 10. Morphological characterization of two layers pressed film.

It is noticed however the presence of small bubbles in the films what is a disadvantage against OLF. These defects can cause a disruption of the sample during the polarisation explained in the work of Navid et al.[61] with the variation in values of resistivity between commercial films with a similar composition of the used in this work, pure films and porous films. This relationship between samples resistivity shows a lower resistivity of a porous film against a commercial one which is related to the presence of pores that will result in a non-uniform electric field in the sample. Another disadvantage of this film is the large thickness of about 100 μm , meaning that it is required a higher electric field to polarise the sample.

The last type of studied films could be a solution to obtain a film with homogeneous surface and without bubbles which may be a problem in the polling process. These films are one layer materials as the OLF but with an ironing treatment, which will smooth the top surface that normally shows more irregularities. The one layer printed film with ironing (OLFI) have the morphology shown in Figure 11, and is a thinner film about 65 μm with a similar appearance of the top and bottom surfaces, even in the

centre what not occur in OLF.

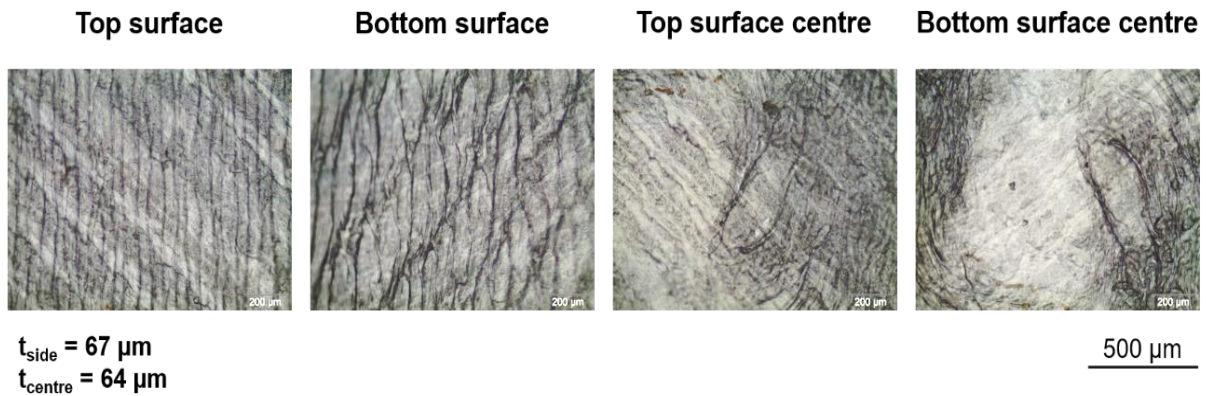


Figure 11. Morphological characterization of one layer printed film with ironing (OLFI).

Looking into the morphological images of three types of produced films and thinking about the complexity of the fabric process of each sample some conclusions can be obtained about which film has the best properties.

The OLF has just the reduced time as an advantage due to the complexity of the process being similar to OLFI and the top surfaces of these films are too much irregular and with a large variety of thickness over the sample. On the other hand, the TLPF has just great homogeneity of surfaces as its main characteristic of the required application for the film. When compared to other films, the TLPF have drawbacks like the need for an extra process to press the films after the 3D printing process. It also has limited to larger thicknesses, due to being a result of pressing two layers of OLF. Lastly, it also has the limitation of the bubbles which can cause a disruption of the material too earlier.

The last presented type of produced films only has one disadvantage that is a longer duration of the 3D printing process. Nevertheless, the increasing time is not relevant in the total printing time of OLFI. On the other hand, these films are made in just one process and with just one equipment, having nice similarities and a uniform displacement in both surfaces, with no significant irregularities. They are the thinnest films when compared with the remaining options. Regarding the analysis of morphology, the OLF is considered a not so good option, which lead to its exclusion in the next characterizations.

2.2. DSC characterization of pellet, fibre, two layers pressed film and one layer film with ironing

The DSC experiment, shown in Figure 12, was made to verify if exists any significant differences in the peak of Curie temperature and fusion temperature in pellet, fibre, TLPF and OLFI. The peaks around 116 °C represent the Curie temperature while the fusion temperature is represented in the peaks around 140 °C. Analysing the results, it is possible to conclude that it does not exist significant differences between the positions of the peaks, which means that during the process the material does not change its properties.

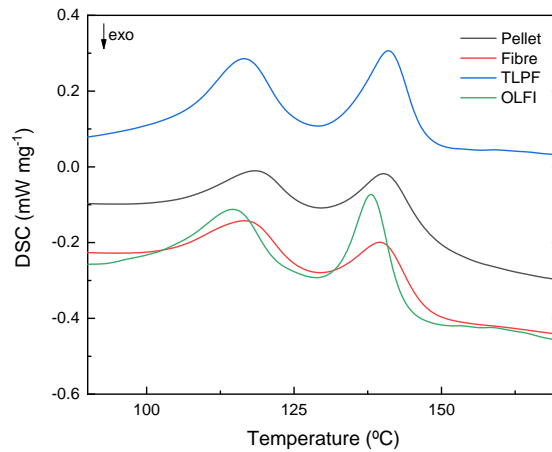


Figure 12. DSC spectra of P(VDF-TrFE) pellet, fibre, TLPF and OLFI.

2.3. FTIR characterization of pellet, fibre, two layers pressed film and one layer film with ironing

To study the crystalline phase of the different stages of P(VDF-TrFE) during the work there were characterized pellets, fibres, TLPF and OLFI via FTIR, shown in Figure 13. The TLPF still needs to be studied in order to understand if it could be a viable option to produce an electroactive device, although showing that the morphology could be a problem in its polarisation.

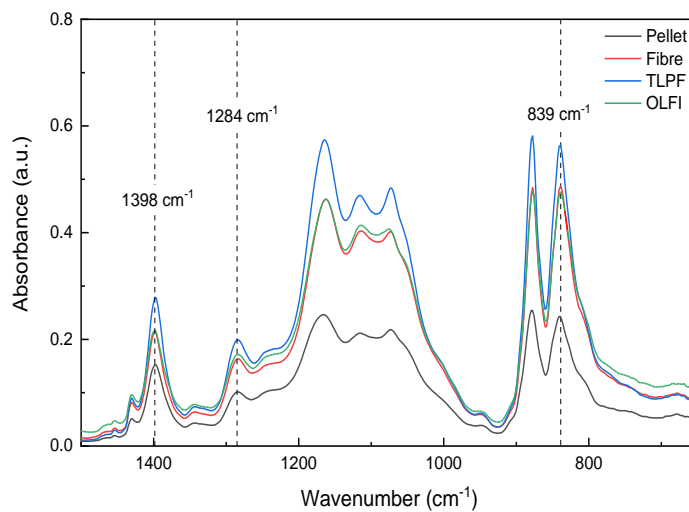


Figure 13. FTIR spectra of P(VDF-TrFE) pellet, fibre, TLPF and OLFI.

Analysing the FTIR spectra it is observed a presence of three characteristic absorption peaks of β phase at 839, 1284 and 1398 cm^{-1} which are related with the P(VDF-TrFE) dipoles orientation. The peak at 1398 cm^{-1} is assigned to CH_2 wagging vibration and symmetric stretching. The peaks with a wavenumber of 839 and 1284 cm^{-1} are assigned to symmetric stretching of CF_2 and CH_2 , respectively. These three characteristic peaks are also related to symmetric stretching of CC. Beyond these characteristic peaks there are two visible intense peaks at 878 and 1164 cm^{-1} related with rocking and asymmetric stretching of CF_2 and rocking of CH_2 only at 878 cm^{-1} . [62], [63]

Comparing the four spectra it is observed a big difference between pellets and the other three, which is related to the fact of pellets do not being submitted to processes with a temperature near to melting

point. This will influence the intensity of the peaks due to the tendency of the copolymer to crystallize in β phase after solidification. When the pellet is transformed in fibre it suffers a melting process which increases the presence of β phase. Using the same logic is observed a small difference between fibre and OLF1 because the second one is submitted to a melting process during the printing process. Nevertheless, the melting and solidifying process of the material is too fast and it does not have a big influence in the phases of the material. As TLPF is submitted to a pressing process using a temperature near to melting point for some time it occurs crystallization in β phase in the solidification.[42], [46]

2.4. XRD characterization of pellet, fibre, two layers pressed film and one layer film with ironing

XRD was done with the main objective of verifying if exists any structural differences between pellet, fibre, TLPF and OLF1. The result of this analysis is shown in Figure 14.

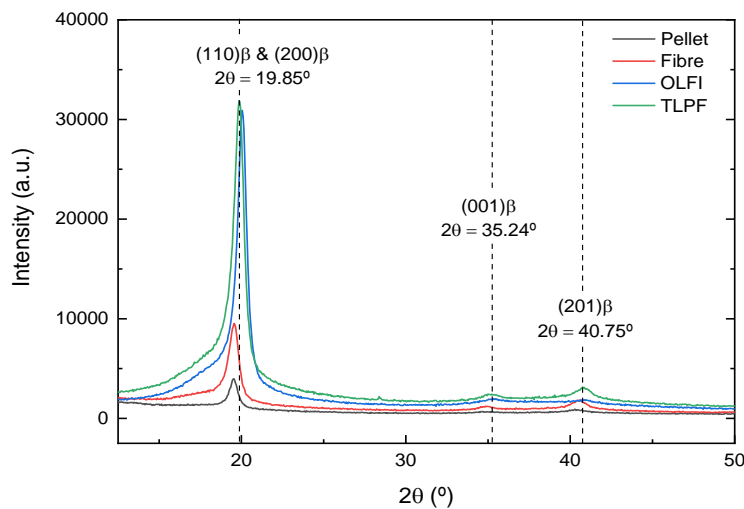


Figure 14. XRD spectra of P(VDF-TrFE) pellet, fibre, TLPF and OLF1.

Accordingly with Oliveira et al.[46] is detected three characteristics peaks of β phase of P(VDF-TrFE) in all samples at 19.85° , 35.24° and 40.75° . The increase of peaks intensity of pellet to TLPF is explained with the use of temperature near to T_c and melting point of the material that was previously explained in FTIR analysis.

The lower intensity curve of fibre when compared with films could be explained with the loss of crystalline structure during the melting process which allows to molecules and atoms to move randomly.[63], [64] Although the films were submitted to temperature, other parameters which influence the crystallinity are the duration of the melting process and the rate of heating and cooling.[46] These parameters explain the higher intensity of peaks of films comparing with fibre because in the production of the second one the material still melting for more time.

The OLF1 uses a higher temperature than in fibre production which could influence the decrease of the peak intensity but analysing the XRD curve this does not happen. The peak of OLF1 is higher than fibre because of the quantity of material that is fed by the 3D printer during the printing is much less than in fibre production. This decreases the cooling time and transforms almost entirely α phase presented in molten material into β phase.[46], [64]

2.5. Summary of two layers pressed film and one layer film with ironing characterization

To select just one type of films to proceed with the electric characterization of the films it was made all the previous experiments as morphological analysis, DSC, FTIR and XRD. With all of these analyses it was observed that the morphology of OLF1 does not have a uniform surface like the TLPF, nevertheless the surface of the second one even has small bubbles. By comparing the two types with DSC it is observed that both are quite similar, and to correlate both using FTIR and XRD it can be noted that TLPF has a slight presence of β phase which is not a substantial difference.

At the end of these analyses, the results show that TLPF and OLF1 have similar properties, however, the bubbles present in TLPF could be more problematic than a slight irregularity of the surface of OLF1. Another advantage of OLF1 against TLPF is the simplicity of the fabric process because the TLPF needs to be pressed after the printing, while the OLF1 is produced in just one step. Due to those reasons the chosen film to be used into electrical characterization is the OLF1.

3. Sample Characterization

In order to study the produced films it was used three different samples configurations, using aluminium electrodes and CPLA electrodes with a different arrangement, as shown in Figure 15. The three types of configurations using an one layer film with ironing. The different configurations are a P(VDF-TrFE) between two evaporated electrodes of aluminium (AOA), an film with a printed electrode of CPLA and another CPLA electrode printed separately (PCOC) and an film between two CPLA electrodes printed separately (COC).

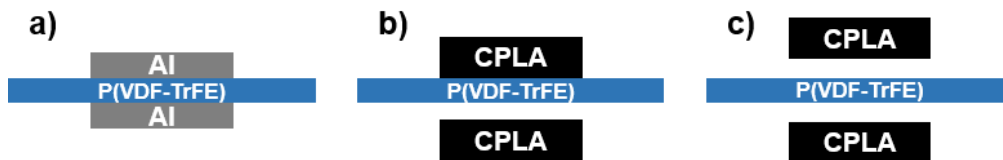


Figure 15. Studied configuration a) AOA, b) PCOC and c) COC.

3.1. Capacitance measurements

The characterization of the samples began with the measurement of the capacitance of the samples to have a better comparison between all configurations before polarization, as shown in Figure 16. In Figure 16 it is also shown the loss tangent ($tg \delta$) of the samples.

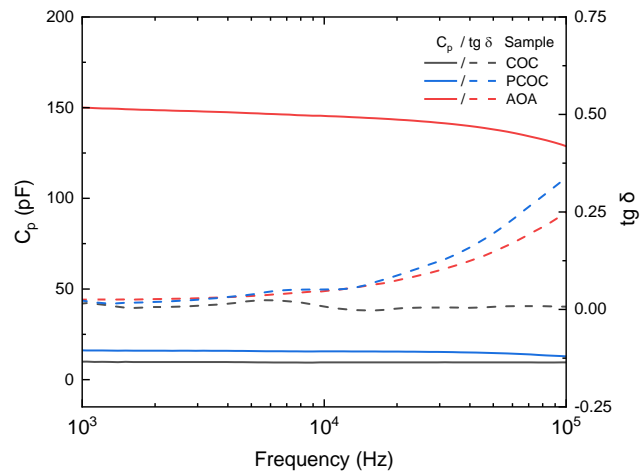


Figure 16. Curves of capacitance (full line) and loss tangent (dash line) of COC, PCOC and AOA configuration.

The measurements performed in AOA configuration at 10 kHz resulted in a capacitance of 146 pF. Due to the unknown area of the electrodes the capacitances of the remaining configurations cannot be considered in the study, once it is necessary to know all the parameters.

In the COC configuration the interfacial surface area between the electrodes and the film was not well defined because the electrodes and the film were independently formed. Subsequently, the way the configuration was assembled influenced the obtained results and it was not possible to know the exact area of the electrodes. In the PCOC configuration it was also not possible to determine the interfacial surface area of the sample and was not ensured the uniformity of the thickness and surface of the film during the printing step. On other hands, the AOA configuration is the one that presents higher capacitance due to the use of the aluminium electrodes. The interfacial surface area is higher which increase the regions where charges can be collected.[65]

Only the AOA configuration presented reliable results. The capacitance of this configuration was used to compare with the theoretical capacitance of P(VDF-TrFE) with a thickness of 65 μm . The theoretical capacitance of 118 pF was determined using the relative permittivity of 11 F m^{-1} presented in material datasheet in Table 1. The two obtained values were very similar which means that the AOA configuration does not affect the electrical properties and response of the material.

The loss tangent in COC configuration is negligible and can be possibly explained by the structure of this sample. In this configuration, the electrodes were made separately from the film which reduces the possibility of affecting the film.

The way the electrodes were built in the PCOC and AOA configurations can affect the integrity of the film and increase the possibility of defects. Hence, these defects can affect the dissipation of the electrical energy which subsequently increases the loss tangent.[66]

3.2. Polarisation experiments

Through configurations tests it was studied which was the electric limit of the sample, testing many samples to understand what would be the breakdown voltage of the films of each structure. The tests performed during the polarisation of COC, PCOC and AOA configuration are shown in Figure 17.

During the test of polarisation it was observed that the COC samples do not tolerate electric fields up to 69 MV m^{-1} , reaching their breakdown voltage. During the tests of bipolar polarisation, shown in Figure 17 (a) there are also visible the expected increasing of the current and the effect of the polarisation in the curves are more evident with the increasing of the applied electric fields. The same relationship between applied electric fields and output current is visible, as shown in Figure 17 (b). In both polarisations it is seen that exists a higher difference between the test at 62 and 69 MV m^{-1} . This can be explained by the imminence of the breakdown voltage of the sample, which will affect much more the mobility of the dipoles and their alignment. The differences of obtained currents between bipolar and unipolar are related with some space charges that will flow into first cycles of unipolar polarisation, decreasing the total current of charge in the inner structure of the material.[67]

The polarisation of the PCOC samples is performed at 54 , 62 and 69 MV m^{-1} as the COC samples. In the bipolar polarisation, shown in Figure 17 (c), it is seen the expected increase of the current with the increasing of the applied electric field, as also the deformation of the curve. On the other hand, the curves of 62 and 69 MV m^{-1} in unipolar polarisation, shown in Figure 17 (d), are very close, being the first one a little higher which needs a detailed study about it. This maybe can be explained by the starting of creation of a negative space charge which reduces the current.[68]

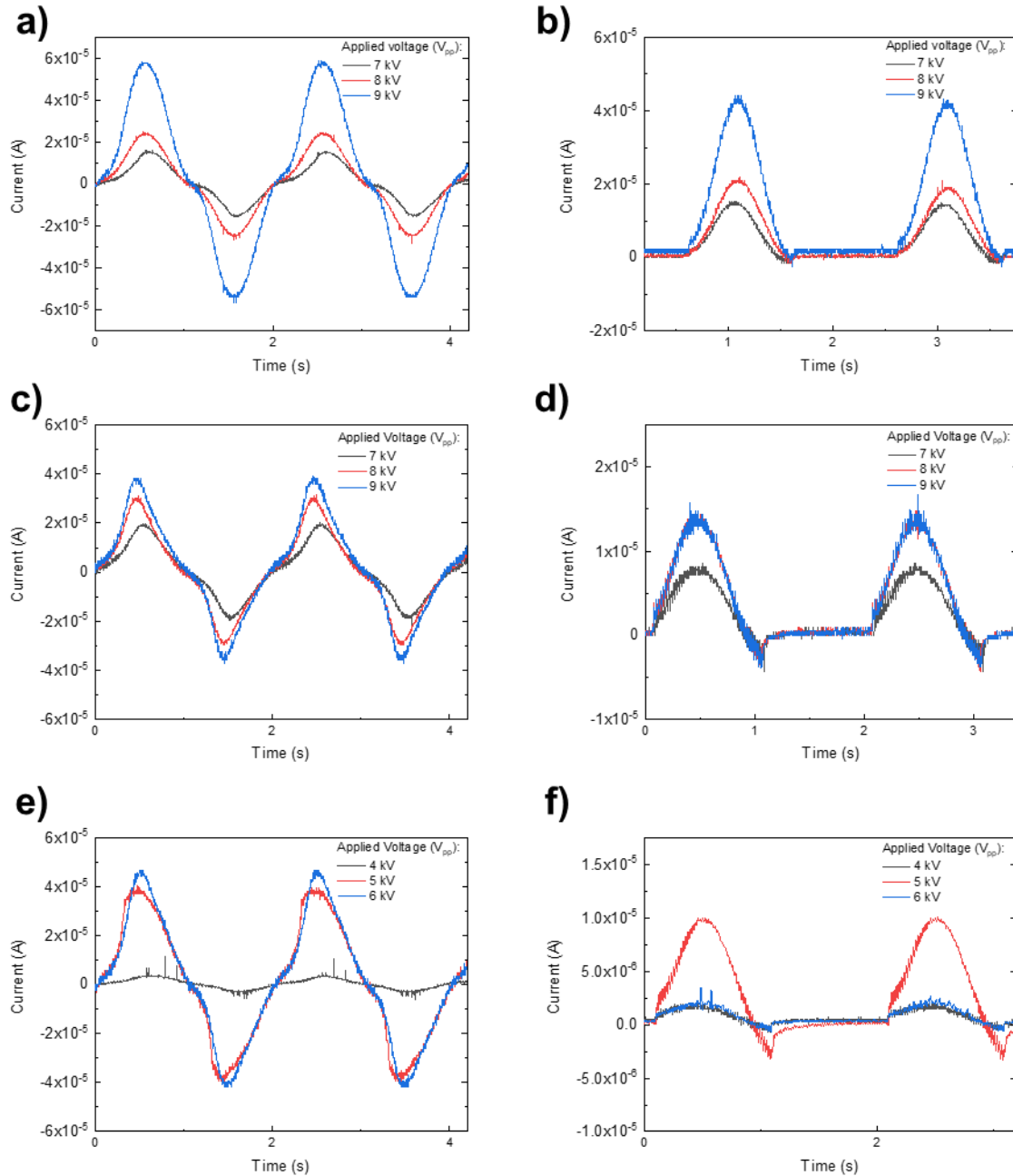


Figure 17. Curve of a) COC bipolar polarisation, b) COC unipolar polarisation, c) PCOC bipolar polarisation, d) PCOC unipolar polarisation, e) AOA bipolar polarisation and f) AOA unipolar polarisation.

The polarisation of AOA configuration samples is made applying 31, 39 and 46 MV m⁻¹, not tolerating higher electric fields, which could be related with higher conductivity of the electrodes used in this structure. In bipolar, as in Figure 17 (e), the perspective of the increasing of the polarisation response with the applied electric field it is confirmed. However, in unipolar polarisation the sample under 46 MV m⁻¹ does not show the expected higher response, otherwise, the response would be similar to the response of the sample under 31 MV m⁻¹. In the unipolar polarisation, Figure 17 (f), the decreasing of the sample current under an electric field of 46 MV m⁻¹ required further studies in future works. Nevertheless, in a first approach it can be explained by the creation of a negative space charge to counteract the excess of charges that are injected in the sample with higher electric field under

breakdown voltage. This negative space charge means that is created a field which will reduce the rate of charge injection, reducing the current which can pass through the sample.[68]

It was performed the hysteresis cycle of each configuration to compare their coercive fields and remanent polarisations. In Figure 18 is presented the samples which exhibit best properties in previous experiments, as the COC sample at 69 MV m^{-1} , PCOC sample at 62 MV m^{-1} and AOA sample at 39 MV m^{-1} .

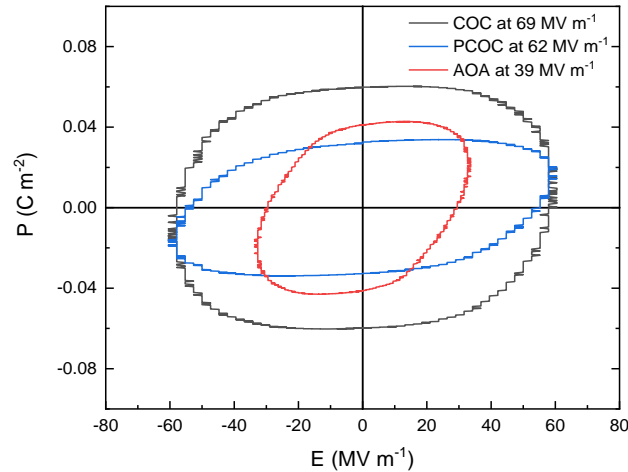


Figure 18. Hysteresis cycle of COC configuration at 69 MV m^{-1} , PCOC configuration at 62 MV m^{-1} and AOA configuration at 39 MV m^{-1} .

From the resulting hysteresis cycle of COC it was obtained the remanent polarisation (P_r) of 0.18 C m^{-2} take it from the polarisation value when the electric field is zero. On the other end, the coercive field (E_c) around 58 MV m^{-1} is obtained when the polarisation is zero.

In PCOC, the samples at 62 and 69 MV m^{-1} show similar pyroelectric properties with the response being obtained during the polarisation. Due to the better response of 62 MV m^{-1} sample it was chosen to study its polarisation and coercive field. With the hysteresis cycle of this configuration it is obtained the P_r of 0.08 C m^{-2} and an E_c around 48 MV m^{-1} .

Finally, from the AOA hysteresis is obtained the remanent polarisation of 0.13 C m^{-2} and a coercive field around 29 MV m^{-1} .

By comparing the coercive field and remanent polarisation, it can be concluded that AOA has the lowest coercive field which is a great feature in polarisation due to its allowance while using lower electric fields. The remanent polarisation is lower than the COC but this difference is not significant while comparing other parameters.

Comparing the previous results with the values presented in datasheet of the copolymer it was observed some differences related to the produced structures. With these structures it was obtained a coercive field lower than 65 MV m^{-1} and a remanent polarisation higher than 0.06 C m^{-2} presented in information about the copolymer. The difference in the obtained values were significant and means that it retained more polarisation and it was required a lower electric field to polarise the same material.

3.3. Pyroelectric coefficient and Figure of Merit

In order to characterize the configurations after the polarisation, is measured the pyroelectric

response of the samples shown in Figure 19, using the generated current and voltage.

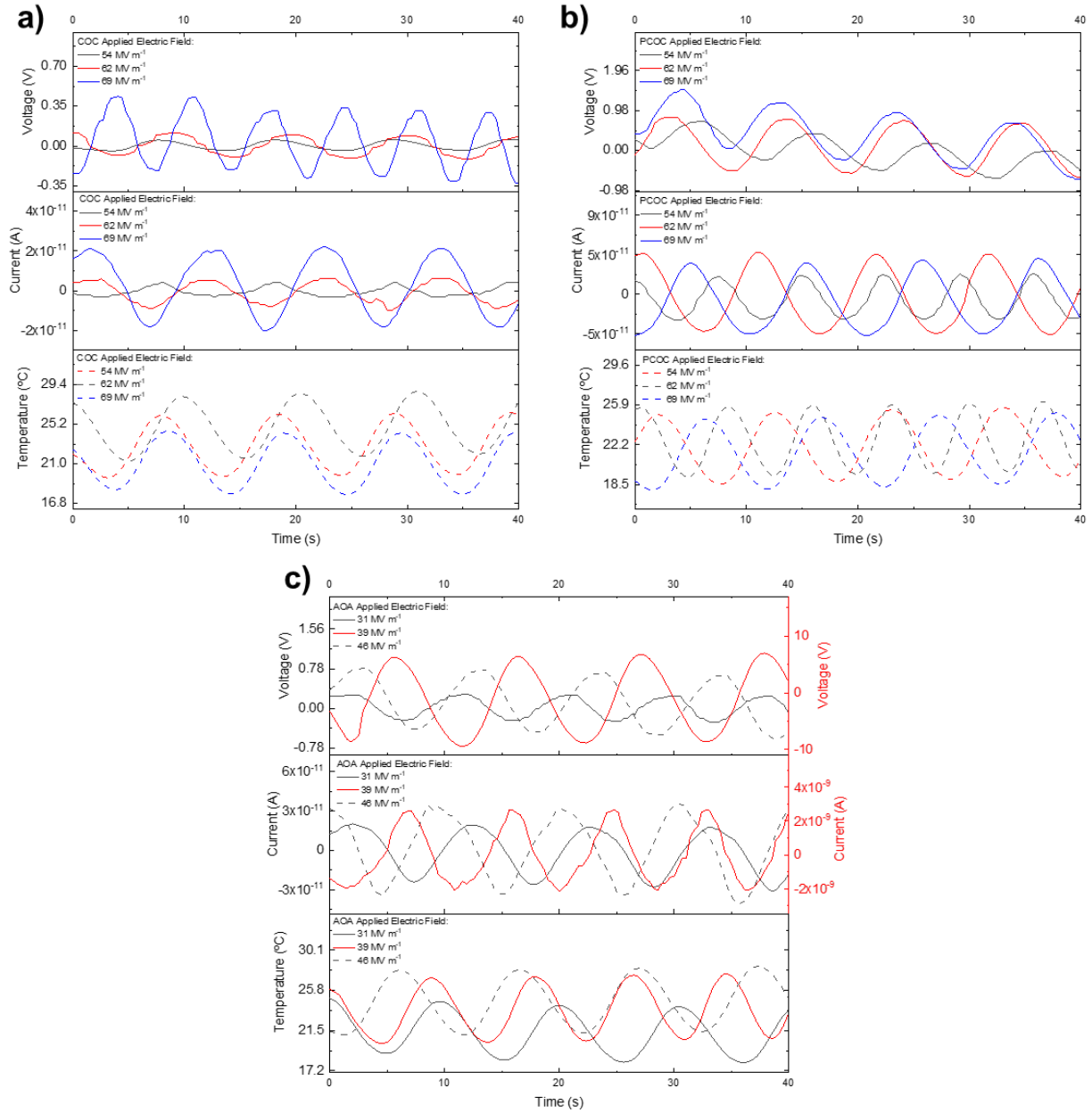


Figure 19. Curve of the pyroelectric response using the generated current and voltage of a) COC configuration, b) PCOC configuration and c) AOA configuration.

Analysing the response of the COC samples, as shown in Figure 19 (a), with different applied electric fields is easily seen that the sample at 69 MV m⁻¹ produces a higher quantity of current when is submitted to a temperature variation. The p_i is calculated using equation 3 and the obtained results are 4.7×10^{-9} , 8.8×10^{-9} and 2.7×10^{-8} C m⁻² K⁻¹ for 54, 62 and 69 MV m⁻¹, respectively.

Considered the values of generated current for the temperature variation of PCOC samples, as in Figure 19 (b), it was calculated the pyroelectric coefficient of 3.5×10^{-8} , 6.2×10^{-8} and 5.8×10^{-8} C m⁻² K⁻¹ for 54, 62 and 69 MV m⁻¹, respectively.

For AOA samples the calculated values of pyroelectric coefficient were 3.2×10^{-8} , 3.3×10^{-6} and 5.3×10^{-8} C m⁻² K⁻¹ for 31, 39 and 46 MV m⁻¹, respectively, expecting that the sample under 39 MV m⁻¹

will show a higher response. This was confirmed and it is shown in Figure 19 (c). The sample submitted to 46 MV m^{-1} is not proportional to the applied voltage in polarisation, which is expected with the previous results in unipolar polarisation and now with these results of pyroelectric response.

It is easily observed the better response of the AOA configuration with the pyroelectric coefficient which is related to the used electrodes. This enables a better uniformity of the electric field that passes through the sample, which influences the alignment of the dipoles without achieving the breakdown voltage too earlier. In the Table 4 is presented the best pyroelectric response of each configuration.

Table 4. Resume of samples characterization.

Sample	Remanent Polarisation (C m^{-2})	Coercive Field (MV m^{-1})	Pyroelectric Coefficient ($\text{C m}^{-2} \text{ K}^{-1}$)
COC at 69 MV m^{-1}	0.18	58	2.7×10^{-8}
PCOC at 62 MV m^{-1}	0.08	48	6.2×10^{-8}
AOA at 39 MV m^{-1}	0.13	29	3.3×10^{-6}

The FOM of AOA sample after polarisation was calculated in order to obtain a better characterization of the studied sample and material. In this study it was used the equation 3 to determine a ϵ_r of 13.7 for AOA after polarisation. The obtained value of F_V for AOA samples after polarisation and was $0.24 \mu\text{C m}^{-2} \text{ K}^{-1}$, by using equation 2. The determined value of the relative permittivity is close to the expected value ($\epsilon_r = 11$), presented in Table 1. The value of F_V is closer to the expected value for this type of polymer when compared to other studies made by Batra et al.[69] and Navid et al.[61].

4. Pyroelectric device experiments

To the experiments of the pyroelectric device are used the AOA configuration because it is the structure which reveals better ferroelectric properties. This experiment was made to understand if the used strategy into the thermal sensor is viable and efficient. In Figure 20 it was possible to observe the response of the AOA sample after polarisation.

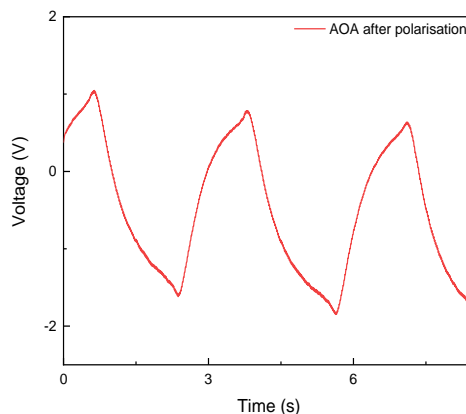


Figure 20. Measurement of device response with AOA film after polarisation.

With the previous results, it is possible to conclude that the produced device exhibits a good response to the applied stimulus of a lamp and confirms the great capabilities of this configuration to be used in full printable pyroelectric sensor.

Chapter IV. Conclusion

This work was developed to study the P(VDF-TrFE) as active material in a pyroelectric sensor. In order to choose the best possible configuration it was characterized by different films and structures before implementing it on a device.

There was studied the sheet resistance of the samples with a different number of layers in order to obtain the best results using CPLA electrodes. It was concluded that the best results were obtained in 4 layers samples with a sheet resistance around $1 \text{ k}\Omega/\square$.

Beyond these electrical properties it was also observed the increase of the fragility of electrodes related with more layers although the decreasing of resistance, being the samples with 4 layers the ones which show best overall results. After choosing the best structure of electrodes it was chosen the OLF1 to be part of the studied configurations because of their advantages against the other films in the structure and homogeneity of the surface which could be a problem in the polarisation.

The OLF1 has other benefits as the lower complexity during the fabrication process which enables the production of good quality films in just one step, the reducing the time of the process and the types of equipment required to create them. In the characterization of the films by DSC, FTIR and XRD were also seen some differences when compared with the pellets and fibre. Comparing the films with the pellets and fibres it has been detected some differences in the quantity of β phase while between the experimented films was not observed significant changes.

The characterization of the produced configurations began with the study of the capacitance of different structures where the AOA shows better results with the obtaining capacitance of 146 pF , which is ten times superior to the other samples capacitance what indicates their good properties.

The samples were polarised and then was observed that the AOA configuration shows a higher pyroelectric response with a coefficient of $3.3 \times 10^{-6} \text{ C m}^{-2} \text{ K}^{-1}$ while the other samples show pyroelectric coefficients one hundred times lower. At this moment, the AOA was showing better results and with the advantage of using lower electric fields to obtain better results.

To complete the characterization it was also analysed the hysteresis cycle of the samples, where the AOA confirmed that it does not require higher fields because it has the lowest coercive field of the studied configurations. It was also performed further experiments to the AOA after polarisation to obtain a better characterization of the structures that were previously chosen to be implemented in a device.

To conclude this work it was experimented a full printable device to test the capabilities of the AOA configuration as a pyroelectric sensor and was confirmed a good response from the device. With this final result it was possible to prove that this concept of producing a full printable sensor is feasible.

There are several studies which would complete this work, being one of them understanding how could it be solved the main problem of fabricating samples with both electrodes directly printed over the film. This problem could be surpassed using a 3D printer with two extruders, to allow the printing of two different materials during the printing process without contaminating the second material which passes through the nozzle with remains of the first material.

This would be the main approach to avoid the using of another type of electrodes because using these printed electrodes is not necessary using evaporation processes which is more expensive and take more time.

To increase the efficiency of the sensors it can be performed a study about other materials or composites to be used as the electrodes. A required result from this study about new materials would be the guarantee about their viability as conductive materials, their capabilities to be used in the printing process and their non-toxicity for the humans.

With these two new approaches and with the intensification of the study about the polarisation attachment into the printing process it will be possible the production of a sensor in just one step, turning this process an easy and scalable way to produce sensors.

References

- [1] D. Stewart, "Telecommunications Predictions 2019 - 3D printing growth accelerates again," *11 December 2018, 2019.* [Online]. Available: <https://www2.deloitte.com/us/en/insights/industry/technology/technology-media-and-telecom-predictions/3d-printing-market.html>.
- [2] E. Matias and B. Rao, "3D printing: On its historical evolution and the implications for business," *Portl. Int. Conf. Manag. Eng. Technol.*, vol. 2015-Sept, pp. 551–558, 2015.
- [3] S. Mishra, L. Unnikrishnan, S. K. Nayak, and S. Mohanty, "Advances in Piezoelectric Polymer Composites for Energy Harvesting Applications : A Systematic Review," vol. 1800463, pp. 1–25, 2019.
- [4] T. N. A. T. Rahim, A. M. Abdullah, and H. Md Akil, "Recent Developments in Fused Deposition Modeling-Based 3D Printing of Polymers and Their Composites," *Polym. Rev.*, vol. 0, no. 0, pp. 1–36, 2019.
- [5] G. D. Goh, S. Agarwala, G. L. Goh, V. Dikshit, S. L. Sing, and W. Y. Yeong, "Additive manufacturing in unmanned aerial vehicles (UAVs): Challenges and potential," *Aerosp. Sci. Technol.*, vol. 63, no. December, pp. 140–151, 2017.
- [6] T. W. Campbell, C. Williams, O. Ivanova, and B. Garrett, "Technologies, Potential, and Implications of Additive Manufacturing," *Atl. Counc.*, 2011.
- [7] G. L. Goh, S. Agarwala, and W. Y. Yeong, "Directed and On-Demand Alignment of Carbon Nanotube: A Review toward 3D Printing of Electronics," *Adv. Mater. Interfaces*, vol. 6, no. 4, 2019.
- [8] R. P. Rimington, A. J. Capel, S. D. R. Christie, and M. P. Lewis, "Biocompatible 3D printed polymers: Via fused deposition modelling direct C2C12 cellular phenotype in vitro," *Lab Chip*, vol. 17, no. 17, pp. 2982–2993, 2017.
- [9] L. Behre, P. Mercorelli, U. Becker, and T. van Niekerk, "Rapid Prototyping of a Mechatronic Engine Valve Controller for IC Engines," *IFAC-PapersOnLine*, vol. 49, no. 21, pp. 54–58, 2016.
- [10] X. Wei *et al.*, "3D Printable Graphene Composite," *Sci. Rep.*, vol. 5, pp. 1–7, 2015.
- [11] A. M. Abdullah, D. Mohamad, T. N. D. T. Din, S. Yahya, H. M. Akil, and Z. A. Rajion, "Fabrication of nasal prosthesis utilising an affordable 3D printer," *Int. J. Adv. Manuf. Technol.*, vol. 100, no. 5–8, pp. 1907–1912, 2019.
- [12] O. S. Carneiro, A. F. Silva, and R. Gomes, "Fused deposition modeling with polypropylene," *Mater. Des.*, vol. 83, pp. 768–776, 2015.
- [13] T. N. A. T. Rahim, A. M. Abdullah, H. M. Akil, D. Mohamad, and Z. A. Rajion, "The improvement of mechanical and thermal properties of polyamide 12 3D printed parts by fused deposition modelling," *Express Polym. Lett.*, vol. 11, no. 12, pp. 963–982, 2017.
- [14] A. Dorigato, V. Moretti, S. Dul, S. H. Unterberger, and A. Pegoretti, "Electrically conductive nanocomposites for fused deposition modelling," *Synth. Met.*, vol. 226, pp. 7–14, 2017.
- [15] G. L. Goh *et al.*, "Additively manufactured multi-material free-form structure with printed electronics," *Int. J. Adv. Manuf. Technol.*, vol. 94, no. 1–4, pp. 1309–1316, 2018.
- [16] J. Huff and P. F. Infante, "Styrene exposure and risk of cancer," *Mutagenesis*, vol. 26, no. 5, pp.

- 583–584, 2011.
- [17] J. M. Anderson and M. S. Shive, “Biodegradation and biocompatibility of PLA and PLGA microspheres,” *Adv. Drug Deliv. Rev.*, vol. 64, no. SUPPL., pp. 72–82, 2012.
- [18] W. Gao *et al.*, “The status, challenges, and future of additive manufacturing in engineering,” *CAD Comput. Aided Des.*, vol. 69, pp. 65–89, 2015.
- [19] S. Bodkhe and P. Ermanni, “Challenges in 3D printing of piezoelectric materials,” *Multifunct. Mater.*, vol. 2, no. 2, p. 22001, 2019.
- [20] Chris Rauwendaal, *Polymer Extrusion*, 5th ed. Hanser Publications, 2014.
- [21] Jörg Breitenbach, “Melt extrusion: from process to drug delivery technology,” *Elsevier Acad. Press*, vol. 54, pp. 107–117, 2002.
- [22] P. Vilarinho, “Scanning Probe Microscopy: Characterization, Nanofabrication and Device Application of Functional Materials,” no. January, Aveiro, 2005.
- [23] Y. Bar-Cohen, *Electroactive polymers as actuators*. Woodhead Publishing Limited, 2010.
- [24] Y. Bar-Cohen and Q. Zhang, “Electroactive Polymer Actuators and Sensors,” *MRS Bull.*, vol. 33, no. 3, pp. 173–181, 2008.
- [25] Y. Bar-Cohen, *Biomimetics: Biologically Inspired Technologies*. Boca Raton: CRC Press, 2006.
- [26] T. Wang *et al.*, “Electroactive polymers for sensing,” *Interface Focus*, vol. 6, no. 4, 2016.
- [27] Y. Bar-Cohen, “Electroactive Polymers as Artificial Muscles - Reality and Challenges,” *19th AIAA Appl. Aerodyn. Conf.*, no. March, 2001.
- [28] H. Kawai, “The Piezoelectricity of Poly (vinylidene Fluoride),” *Jpn. J. Appl. Phys.*, vol. 8, no. 7, pp. 975–976, 1969.
- [29] J. G. Bergman, J. H. McFee, and G. R. Crane, “Pyroelectricity and optical second harmonic generation in polyvinylidene fluoride films,” *Appl. Phys. Lett.*, vol. 18, no. 5, pp. 203–205, 1971.
- [30] Q. Li and Q. Wang, “Ferroelectric Polymers and Their Energy-Related Applications,” *Macromol. Chem. Phys.*, vol. 217, no. 11, pp. 1228–1244, 2016.
- [31] R. W. Whatmore, “Pyroelectric devices and materials,” *Reports Prog. Phys.*, vol. 49, no. 12, pp. 1335–1386, 1986.
- [32] P. Mane, J. Xie, K. K. Leang, and K. Mossi, “Cyclic energy harvesting from pyroelectric materials,” *IEEE Trans. Ultrason. Ferroelectr. Freq. Control*, vol. 58, no. 1, pp. 10–17, 2011.
- [33] C. R. Bowen, J. Taylor, E. Le Boulbar, D. Zabek, A. Chauhan, and R. Vaish, “Pyroelectric materials and devices for energy harvesting applications,” *Energy Environ. Sci.*, vol. 7, no. 12, pp. 3836–3856, 2014.
- [34] D. Ando, F. Eichhorn, T. Fey, and K. ichi Kakimoto, “Secondary Pyroelectric Effect and Figure of Merit of Ferroelectric 0–3 Composites,” *Adv. Eng. Mater.*, vol. 21, no. 6, pp. 1–5, 2019.
- [35] C. Li, P. M. Wu, L. A. Shutter, and R. K. Narayan, “Dual-mode operation of flexible piezoelectric polymer diaphragm for intracranial pressure measurement,” *Appl. Phys. Lett.*, vol. 96, no. 5, pp. 1–4, 2010.
- [36] C. Li, P. M. Wu, S. Lee, A. Gorton, M. J. Schulz, and C. H. Ahn, “Flexible dome and bump shape piezoelectric tactile sensors using PVDF-TrFE copolymer,” *J. Microelectromechanical Syst.*, vol. 17, no. 2, pp. 334–341, 2008.

- [37] F. Maita *et al.*, "Ultraflexible Tactile Piezoelectric Sensor Based on Low-Temperature Polycrystalline Silicon Thin-Film Transistor Technology," *IEEE Sens. J.*, vol. 15, no. 7, pp. 3819–3826, 2015.
- [38] W. Y. Chang, C. H. Chu, and Y. C. Lin, "A flexible piezoelectric sensor for microfluidic applications using polyvinylidene fluoride," *IEEE Sens. J.*, vol. 8, no. 5, pp. 495–500, 2008.
- [39] S. Hannah, A. Davidson, I. Glesk, D. Uttamchandani, R. Dahiya, and H. Gleskova, "Multifunctional sensor based on organic field-effect transistor and ferroelectric poly(vinylidene fluoride trifluoroethylene)," *Org. Electron. physics, Mater. Appl.*, vol. 56, no. February, pp. 170–177, 2018.
- [40] S. Crossley, R. A. Whiter, and S. Kar-Narayan, "Polymer-based nanopiezoelectric generators for energy harvesting applications," *Energy Mater. Mater. Sci. Eng. Energy Syst.*, vol. 9, no. 3, pp. 1613–1624, 2014.
- [41] J. H. Lee *et al.*, "Micropatterned P(VDF-TrFE) film-based piezoelectric nanogenerators for highly sensitive self-powered pressure sensors," *Adv. Funct. Mater.*, vol. 25, no. 21, pp. 3203–3209, 2015.
- [42] P. Martins, A. C. Lopes, and S. Lanceros-Mendez, "Electroactive phases of poly(vinylidene fluoride): Determination, processing and applications," *Prog. Polym. Sci.*, vol. 39, no. 4, pp. 683–706, 2014.
- [43] P. Costa, J. Nunes-Pereira, N. Pereira, N. Castro, S. Gonçalves, and S. Lanceros-Mendez, "Recent Progress on Piezoelectric, Pyroelectric, and Magnetoelectric Polymer-Based Energy-Harvesting Devices," *Energy Technol.*, vol. 7, no. 7, pp. 1–19, 2019.
- [44] A. Salimi and A. A. Yousefi, "FTIR studies of β -phase crystal formation in stretched PVDF films," *Polym. Test.*, vol. 22, no. 6, pp. 699–704, 2003.
- [45] L. Ruan, X. Yao, Y. Chang, L. Zhou, G. Qin, and X. Zhang, "Properties and applications of the β phase poly(vinylidene fluoride)," *Polymers (Basel)*, vol. 10, no. 3, pp. 1–27, 2018.
- [46] F. Oliveira, Y. Leterrier, O. Sereda, A. Neels, A. Dommann, and D. Damjanovic, "Process influences on the structure, piezoelectric, and gas-barrier properties of PVDF-TrFE copolymer," *J. Polym. Sci. Part B Polym. Phys.*, vol. 52, no. 7, pp. 496–506, 2014.
- [47] A. J. Lovinger, D. D. Davis, R. E. Cais, and J. M. Kometani, "The role of molecular defects on the structure and phase transitions of poly(vinylidene fluoride)," *Polymer (Guildf)*, vol. 28, no. 4, pp. 617–626, 1987.
- [48] T. Yamada, T. Ueda, and T. Kitayama, "Ferroelectric-to-paraelectric phase transition of vinylidene fluoride-trifluoroethylene copolymer," *J. Appl. Phys.*, vol. 52, no. 2, pp. 948–952, 1981.
- [49] E. Fukada, "History and Recent Progress in piezoelectric polymers," *Ieee Transduct. Ultrason. Freq. Control*, vol. 47, no. 6, pp. 1277–1289, 2000.
- [50] L. Zhu, "Exploring strategies for high dielectric constant and low loss polymer dielectrics," *J. Phys. Chem. Lett.*, vol. 5, no. 21, pp. 3677–3687, 2014.
- [51] J. Watanabe, K. Imai, and I. Uematsu, "On the Curie temperature of poly(vinylidene fluoride)," *Am. Chem. Soc.*, pp. 1491–1494, 1986.
- [52] J. X. Wen *et al.*, "Piezoelectric Polymers – Materials and Manufacture," *Jpn. J. Appl. Phys.*, vol.

- 24, no. 24–2, pp. 23–27, 1985.
- [53] K. Kimura and H. Ohigashi, “Polarization Behavior in Vinylidene Fluoride-Trifluoroethylene Copolymer Thin Films,” *Jpn. J. Appl. Phys.*, vol. 25, pp. 383–387, 1986.
- [54] K. S. Ramadan, D. Sameoto, and S. Evoy, “A review of piezoelectric polymers as functional materials for electromechanical transducers,” *Smart Mater. Struct.*, vol. 23, no. 3, 2014.
- [55] H. Kim, T. Fernando, M. Li, Y. Lin, and T. B. Tseng, “Fabrication and characterization of 3D printed BaTiO₃ / PVDF nanocomposites,” *J. Compos. Mater.*, 2017.
- [56] C. Lee and J. A. Tarbuton, “Electric poling-assisted additive manufacturing process for PVDF polymer- based piezoelectric device applications,” *Smart Mater. Struct.*, vol. 095044, 2014.
- [57] H. Kim, F. Torres, D. Villagran, C. Stewart, Y. Lin, and T. L. B. Tseng, “3D Printing of BaTiO₃/PVDF Composites with Electric In Situ Poling for Pressure Sensor Applications,” *Macromol. Mater. Eng.*, vol. 302, no. 11, pp. 1–6, 2017.
- [58] H. Kim, F. Torres, Y. Wu, and D. Villagran, “Integrated 3D printing and corona poling process of PVDF piezoelectric films for pressure sensor application,” *Smart Mater. Struct.*, vol. 26, no. 8, pp. 085027/1-085027/9, 2017.
- [59] M. Marandi and J. Tarbuton, “Additive manufacturing of single- and double-layer piezoelectric PVDF-TrFE copolymer sensors,” *Procedia Manuf.*, vol. 34, pp. 666–671, 2019.
- [60] D. K. Schroder, *Semiconductor Material and Device Characterization: Third Edition*. 2005.
- [61] A. Navid, C. S. Lynch, and L. Pilon, “Purified and porous poly(vinylidene fluoride-trifluoroethylene) thin films for pyroelectric infrared sensing and energy harvesting,” *Smart Mater. Struct.*, vol. 19, no. 5, 2010.
- [62] J. A. D. S. Æ. C. J. L. Constantino, “Thermomechanical characterization of PVDF and P (VDF-TrFE) blends containing corn starch and natural rubber,” pp. 621–629, 2010.
- [63] R. I. Mahdi, W. C. Gan, and W. H. Abd Majid, “Hot plate annealing at a low temperature of a thin ferroelectric P(VDF-TrFE) film with an improved crystalline structure for sensors and actuators,” *Sensors (Switzerland)*, vol. 14, no. 10, pp. 19115–19127, 2014.
- [64] H. L. W. Chan, Z. Zhao, K. W. Kwok, and C. L. Choy, “Enhancement of piezoelectric activity in P(VDF-TrFE) copolymer using two-step poling,” *8th Int. Symp. Electrets, ISE 1994 - Proc.*, pp. 583–588, 1994.
- [65] R. Ahmed and K. Reifsnider, “Study of influence of electrode geometry on impedance spectroscopy,” *ASME 2010 8th Int. Conf. Fuel Cell Sci. Eng. Technol. FUELCELL 2010*, vol. 2, pp. 1–9, 2010.
- [66] M. T. Sebastian, “Measurement of microwave dielectric properties and factors affecting them,” *Dielectr. Mater. Wirel. Commun.*, pp. 11–47, 2008.
- [67] J. Hornak, P. Trnka, P. Totzauer, and M. Gutten, “The effect of space charge accumulation in high voltage insulation systems,” *Proc. 2017 18th Int. Sci. Conf. Electr. Power Eng. EPE 2017*, 2017.
- [68] K. C. Kao, *Dielectric Phenomena in Solids: With Emphasis on Physical Concepts of Electronic Processes*. Manitoba, 2004.
- [69] A. K. Batra, J. Corda, P. Guggilla, M. D. Aggarwal, and M. E. Edwards, “Dielectric and

pyroelectric properties of LiTaO₃:P(VDF-TrFE) composite films," *Org. Photonic Mater. Devices XI*, vol. 7213, p. 721313, 2009.

- [70] R. Igreja, "Desenvolvimento de materiais compósitos polímero cerâmica para sensores electroactivos," MSc at Faculdade de Ciências e Tecnologia, Universidade Nova de Lisboa, 1997.
- [71] C. J. Dias, "Ferroelectric Composites for Pzrp-And Piezoelectric Applications," PhD at University of Wales, Bangor, UK, 1994.

Appendices

A. PVDF and P(VDF-TrFE) molecular structures

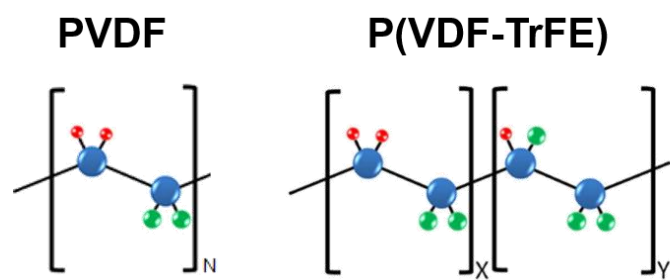


Figure 21. PVDF and P(VDF-TrFE) molecular structures.

B. Additional information about used materials

Table 5. Additional properties of Solvене®250 EAP from SOLVAY SPECIALTY POLYMERS ITALY S.p.A..

Properties	Solvене®250 EAP	Unit
Tensile Strength at Break	49.0 - 54.0	MPa
Tensile Strength, Yield	22.0 - 28.0	MPa
Elongation at Break	400 - 600	%
Elongation at Yield	9.0 - 12	%
Tensile Modulus	0.550 - 0.850	GPa
MFI	35	g/10 min
Crystallization temperature	120	°C
Glass transition	-37	°C
Density	1.7	g cm ⁻³
Modulus	1,000	MPa
Poling field (min)	150	V μm ⁻¹
Poling field (max)	250	V μm ⁻¹
Remnant polarization (max)	> 6	μC cm ⁻²
Breakdown voltage	> 280	V μm ⁻¹

Table 6. Additional properties of Conductive PLA Proto-Pasta from Protoplant.

Properties	Conductive PLA Proto-Pasta	Unit
Resistivity volumetric filament without 3D printing	15	Ω cm ⁻¹
Resistivity volumetric 3D printed parts perpendicular to the layers	30	Ω cm ⁻¹
Density	1.24	g cm ⁻³
Printing temperature	195-225	°C
Print bed temperature	50-60	°C

Table 7. CAS Number of used materials.

Material	CAS Number
Solvене® 250 EAP (P(VDF-TrFE))	28960-88-5
Conductive PLA Proto-Pasta	PLA
	Carbon black
	9051-89-2
	1333-86-4

C. Parameters of 3D printing

Table 8. Parameters used in Ultimaker Cura 4.0.0

Parameter	Unit	P(VDF-TrFE) film	Conductive PLA Proto-Pasta electrodes
Quality	Layer Height	mm	0.06
	Line Width	mm	0.3
	Wall Line Width	mm	0.06
Shell	Wall Thickness	mm	7.3
	Enable Ironing	-	Yes
	Ironing Pattern	-	Zig Zag
	Ironing Flow	%	10
	Ironing Speed	mm s ⁻¹	2
Infill	Infill Density	%	100
Speed	Print Speed	mm s ⁻¹	10
	Infill Speed	mm s ⁻¹	10
	Wall Speed	mm s ⁻¹	10
	Inner Wall Speed	mm s ⁻¹	15
	Top/Bottom Speed	mm s ⁻¹	3
	Initial Layer Speed	mm s ⁻¹	10
	Skirt/Brim Speed	mm s ⁻¹	15

D. Rectifying circuit used in polarisation setup

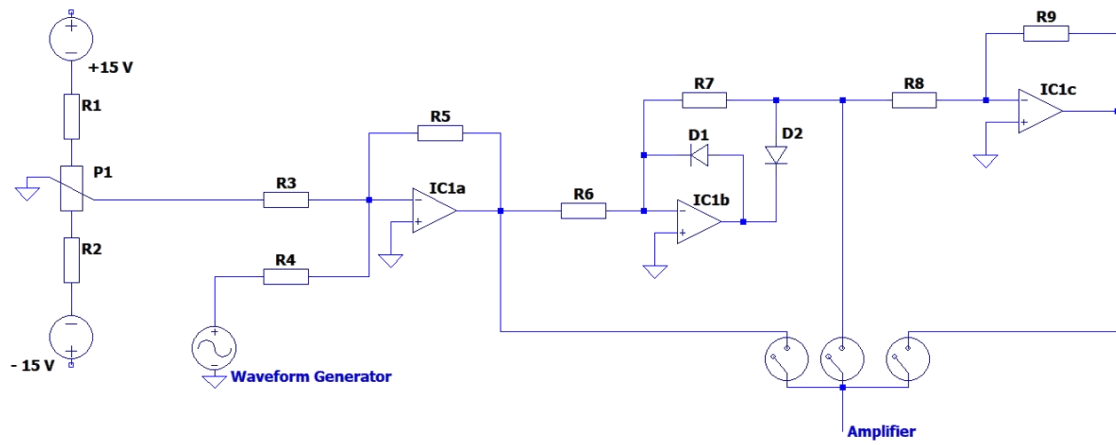


Figure 22. Electric circuit for rectification and control of input signal on the amplifier.[70], [71]

E. Measurement circuit used during the polarisation

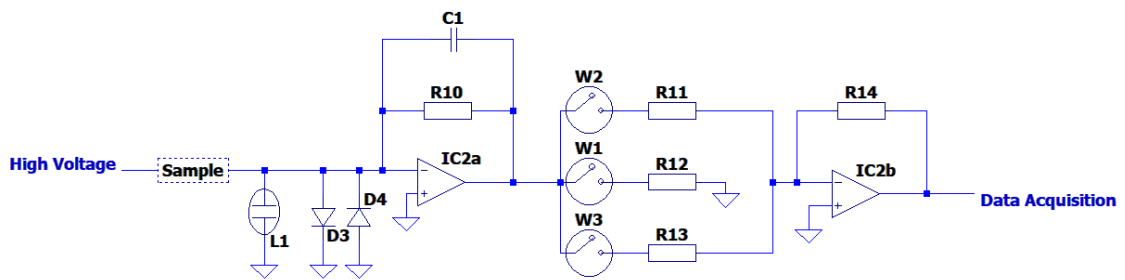


Figure 23. Electric circuit to the measurement of the sample current during the polarisation.[70], [71]

F. Polarisation process

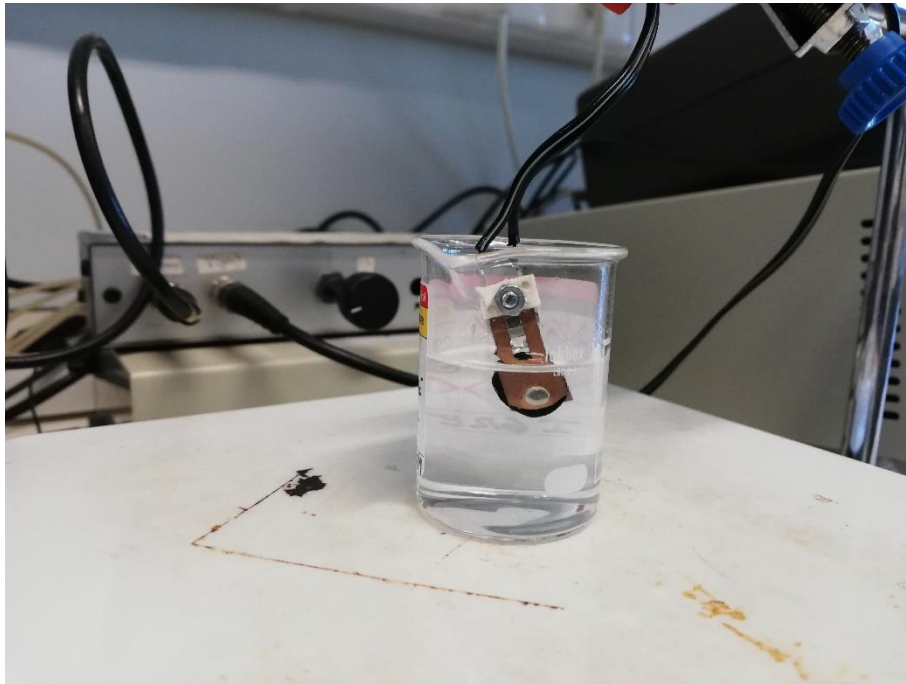


Figure 24. Sample during polarisation in a silicon bath at 90 °C.

G. Measurement of pyroelectric response

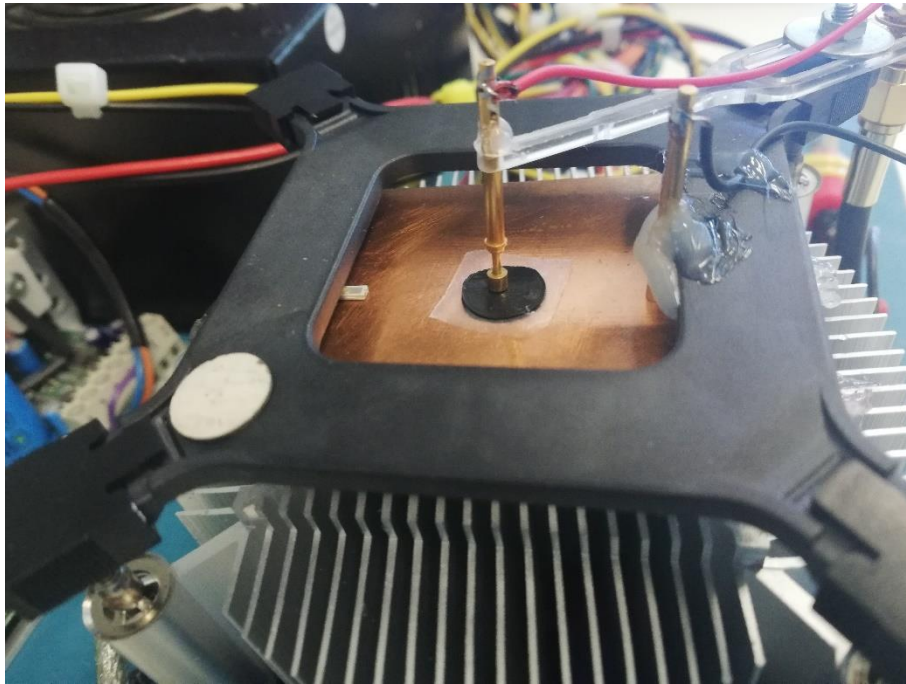


Figure 25. Sample during the measurement of pyroelectric response.

H. Measurement of capacitance

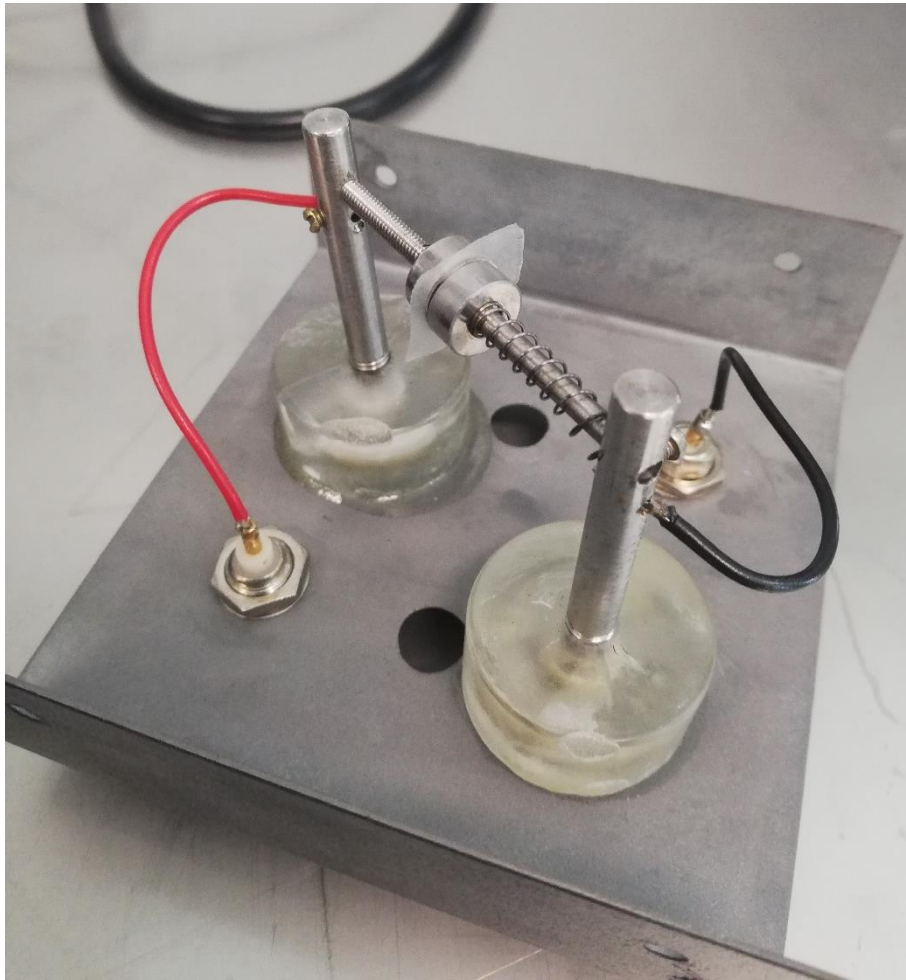


Figure 26. Used setup in capacitance measurements.

I. 3D model device

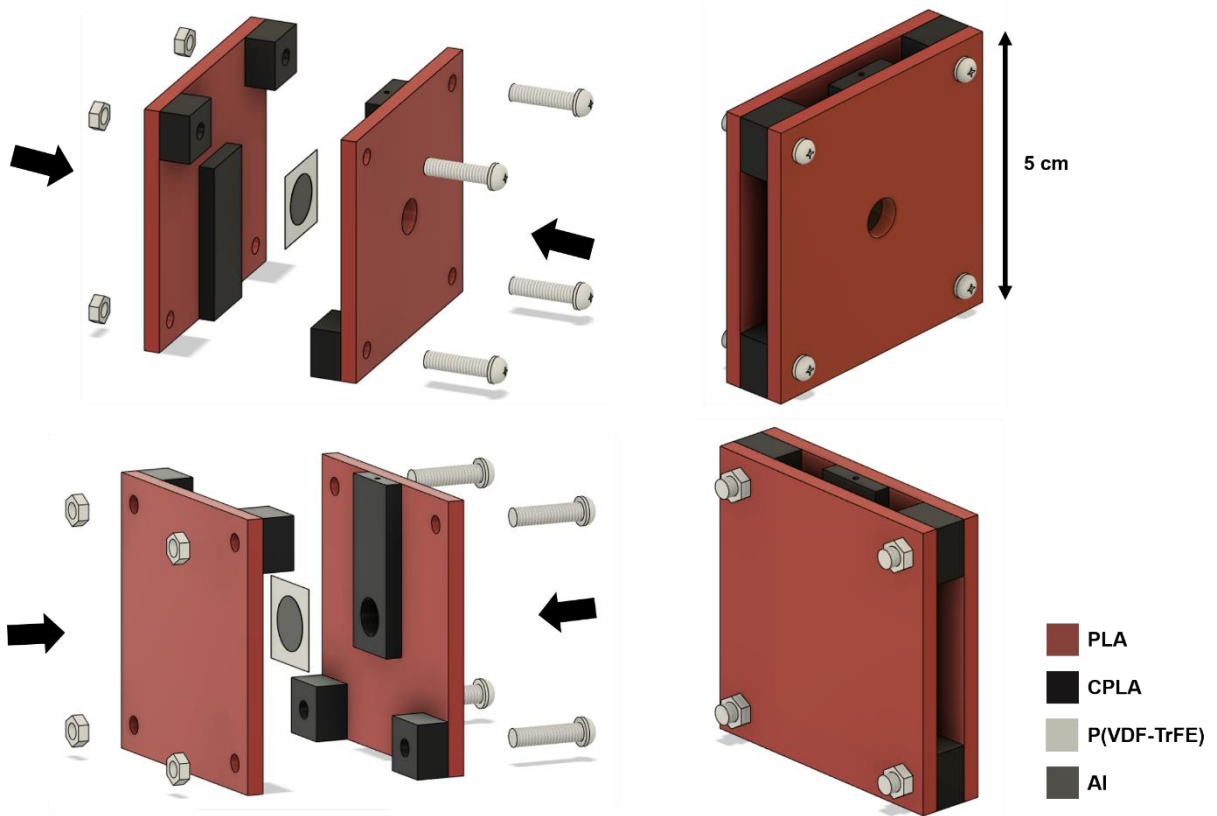


Figure 27. 3D model device.

J. Experimental setup

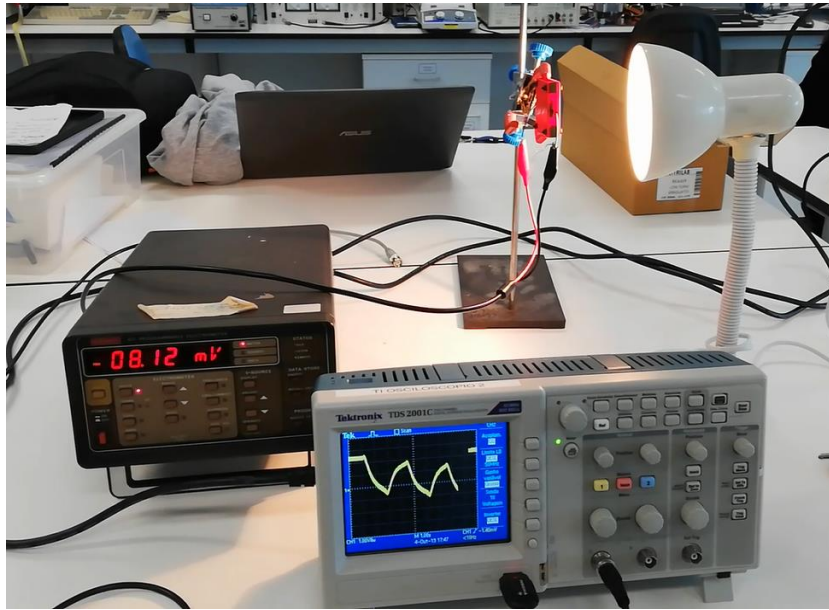


Figure 28. Testing the device providing an heat source.

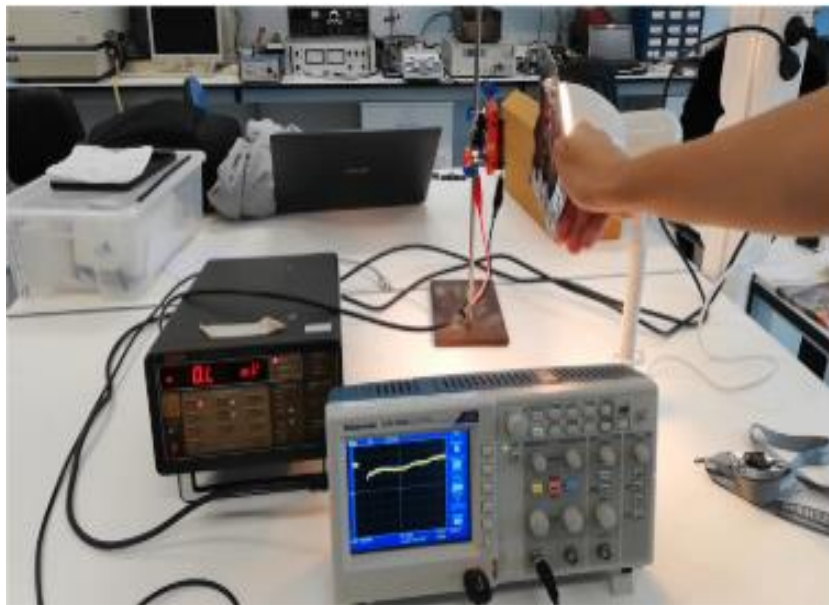


Figure 29. Testing the device in absence of an heat source.

K. Morphological analysis of sheet resistance samples

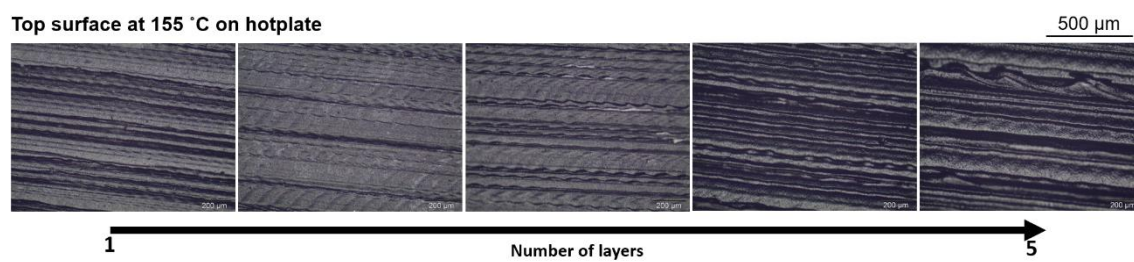


Figure 30. Top surface of sheet resistance samples dried at 155 °C on the hotplate.